



Research Paper

Indium-doped Co_3O_4 nanorods for catalytic oxidation of CO and C_3H_6 towards diesel exhaustLei Ma^a, Chang Yup Seo^a, Xiaoyin Chen^a, Kai Sun^b, Johannes W. Schwank^{a,*}^a Department of Chemical Engineering, University of Michigan, Ann Arbor, MI 48109, USA^b Department of Materials Science and Engineering, University of Michigan, Ann Arbor, MI 48109, USA

ARTICLE INFO

Keywords:

Catalytic oxidation
Synergistic effects
Reaction mechanism
Kinetic study
In situ DRIFTS

ABSTRACT

Platinum-group metals are widely used as diesel oxidation catalysts (DOCs) for exhaust control. It is a challenge to improve performance and reduce the cost of DOCs, while also to avoid interference of hydrocarbons and sintering of platinum metals at high temperatures. We present here an indium-doped Co_3O_4 uniform nanorod catalyst whose catalytic performance in CO, C_3H_6 , and even NO oxidation is comparable to platinum-group DOCs in diesel exhaust. No obvious deactivation was observed in long-term stability tests under simulated diesel exhaust conditions. These indium-doped Co_3O_4 nanorods might open a promising pathway towards low-cost efficient diesel exhaust control systems. Characterization results indicated that lattice oxygen could be much more easily abstracted by hydrogen or carbon monoxide from indium-doped Co_3O_4 than from Co_3O_4 and the physical mixture Co_3O_4 and In_2O_3 . The presence of indium with its large cation radius could influence the chemical status of surface/chemisorbed oxygen in Co_3O_4 - In_2O_3 nanorods, thereby increasing the mobility of lattice oxygen involved in the catalytic oxidation reaction. The reaction mechanism of catalytic oxidation of CO and C_3H_6 were evaluated based on kinetic and FTIR studies. For CO oxidation, activated CO_3^* reduced by adsorbed CO^* in an irreversible step to generate the final product of CO_2 could be considered as the kinetically-relevant step. DRIFT spectroscopy confirmed that only stable carbonate species were observed over Co_3O_4 - In_2O_3 nanorods that might be further reduced by CO to form CO_2 . For C_3H_6 oxidation, the incorporation of activated oxygen (O^*) into anion vacancy of catalyst surface was the kinetically-relevant step, while the active sites on catalyst surface should be totally covered by the intermediates of C_3H_6 or its generated species, which actually acted as the most abundant surface intermediates (MASI). DRIFT spectroscopy confirmed that C_3H_6 and its related intermediates like formate, acetate, and acetone species would be formed over Co_3O_4 - In_2O_3 nanorods.

1. Introduction

Diesel oxidation catalysts (DOCs), usually comprised of supported platinum (Pt) metals, are principally used to oxidize carbon monoxide (CO) and hydrocarbons (HCs) in diesel emissions [1]. In addition, catalytic oxidation of nitrogen oxide (NO) to nitrogen dioxide (NO_2) over DOCs also plays a key role in the effectiveness of NO_x removal including lean NO_x trap (LNT), selective catalytic reduction of NO_x with ammonia (NH_3 -SCR) at low temperatures, and passive regeneration of downstream diesel particulate filters (DPF). Although platinum-group metals are currently the predominant catalyst components in commercial DOCs, there are still some problems with the usage of them [1]. For example, trace amounts of platinum could migrate from heated DOCs to downstream zeolite SCR catalysts, and cause severe performance loss on the zeolite [2], although adding palladium (Pd) could to some extent alleviate this problem. Furthermore, CO oxidation would be severely

inhibited by hydrocarbons due to the strong chemisorption of hydrocarbons on active Pt sites [3]. Pt-group metals are susceptible to sinter causing activity loss at high temperatures [4]. Additionally, the high cost of platinum group metals provides a strong incentive to look for replacements of platinum metals in advanced aftertreatment systems. Therefore, there is substantial interest in developing active DOCs with low noble metal loadings or even noble metal-free DOCs that address the exhaust system cost and meet the target emission regulations.

Several significant studies have been undertaken for developing new generations of noble metal-free DOCs like NO oxidation catalysts comprised of $\text{La}_{1-x}\text{Sr}_x\text{CoO}_3$ [5] and Mn-Mullite [6], but these kinds of catalysts might still have to be combined with Pt or Pd to achieve effective oxidation of CO and HCs in diesel exhaust. Cobalt oxide (Co_3O_4) spinels might be one of the most active oxidation catalysts in automotive emissions control [7–9]. Binder et al. [10] reported that Co_3O_4 doped with copper and ceria could outperform Pt catalysts in CO

* Corresponding author.

E-mail addresses: leima04@gmail.com (L. Ma), schwank@umich.edu (J.W. Schwank).

oxidation at low temperatures in simulated diesel emissions. The advantage of the cobalt ternary oxide catalysts was that CO oxidation would not be significantly inhibited in the presence of propylene (C_3H_6). Yet, the C_3H_6 oxidation performance was still significantly lower than that of as-prepared Pd catalysts and commercial DOCs. In view of these results, the challenge still remains to develop a noble metal-free catalyst capable of effectively handling all the pollutants in diesel exhaust gas mixtures.

It turns out that Co_3O_4 nanorods could maximally expose the effective lattice planes for catalytic oxidation. The surface of Co_3O_4 nanorods exposing (110) lattice planes predominately comprised of Co^{3+} sites, which are generally recognized as the active sites for catalytic oxidation reaction [11]. It is also possible to modify the textural and redox properties of Co_3O_4 and facilitate the formation of oxygen vacancies by introducing metal dopants with different cation radius, which would be much more beneficial for catalytic oxidation [12,13]. Herein, we present a platinum-free catalyst based on indium-doped Co_3O_4 nanorods, which could effectively oxidize CO, propylene, and even NO in simulated diesel exhausts and also exhibit a good long-term stability in the presence of stream. This new class of catalysts might open a promising pathway towards low-cost efficient diesel exhaust control systems that are entirely free of noble metals.

2. Experimental

2.1. Preparations of catalysts

The synthesis of the SBA-15 template followed the procedures reported in the literature [14–16]. The SBA-15 template was prepared in aqueous solution using Pluronic P123 (Sigma Aldrich, average $M_n \sim 5800$) as structure-directing agent and tetraethyl orthosilicate (TEOS, Sigma Aldrich, 98%) as the silicon source. Typically, 10 g P123 was dissolved in 374 mL deionized water and 16 mL HCl (Sigma Aldrich, 37 wt%). The aqueous mixture was heated to 35 °C and vigorously stirred for one hour, after which 21 g TEOS was added into the solution and further left vigorously stirring at 35 °C for 24 h. The solution was subsequently aged at 100 °C for 24 h in autoclaves under static conditions. The solid product was filtered and washed with a mixture of 20 mL HCl and 200 mL ethanol, followed by deionized water wash. It was then finally calcined in static air at 550 °C for 4 h to remove the copolymer template.

Co_3O_4 and In_2O_3 nanorod samples were prepared using SBA-15 silica as a hard template. In a typical synthesis, 1 g of SBA-15 was dispersed in 5 mL of 0.8 M $Co(NO_3)_2 \cdot 6H_2O$ (Sigma Aldrich, ACS reagent, $\geq 98\%$) or 0.8 M $In(NO_3)_3 \cdot xH_2O$ (Sigma Aldrich, 99.99% trace metals basis) in ethanol solution and vigorously stirred at room temperature for at least 4 h. Subsequently, the samples were dried at 60 °C overnight, after which they were transferred to quartz boats without cover followed by a calcination process in static air at a ramp rate of 1 °C/min to 200 °C and held for 4 h. The composite powders were impregnated by metal precursors one more time using the same procedure as that in the first impregnation process, dried at 60 °C overnight, and then calcined at 600 °C for 6 h at a ramp rate of 1 °C/min with an intermediate temperature plateau at 200 °C for 4 h. The silica template was removed by rinsing with 2 M NaOH hot aqueous solution (ca. 80 °C) for at least three times. The solid products were filtered and washed with deionized water until neutralization, dried in an oven at 60 °C overnight, and then treated in flowing nitrogen ($1.67 \text{ cm}^3 \text{ g}^{-1} \text{ s}^{-1}$) with a ramp rate of 1 °C/min to 300 °C and held for 1 h.

Indium-doped Co_3O_4 nanorods, coded as $Co_3O_4-In_2O_3$, were prepared following the same procedure as Co_3O_4 nanorods. During the impregnation process, both $Co(NO_3)_2 \cdot 6H_2O$ and $In(NO_3)_3 \cdot xH_2O$ precursors were dissolved in ethanol solution. The total concentration of metal nitrate precursors was kept at 0.8 M, and the expected mole ratio of Co/In was 5.8. To confirm the synergistic roles between cobalt oxides

and indium oxides, a physical mixture of Co_3O_4 and In_2O_3 nanorods was also prepared and coded as $Co_3O_4 \& In_2O_3$ (26 wt% In_2O_3). The catalyst was used for catalytic oxidation of CO tests and temperature-programmed reduction by hydrogen to examine what role the proximity of cobalt and indium played in $Co_3O_4-In_2O_3$ nanorods. The quantitative results of different elements on $Co_3O_4-In_2O_3$ were analyzed by inductively coupled plasma optical emission spectrometry (ICP-OES) in Galbraith Laboratories, Inc.

All the nanorod powder samples were pressed into pellets and sieved with mesh sizes of 180–250 μm before performing catalytic activity tests and kinetic studies. Before the catalytic tests, all the nanorod samples were pretreated at 300 °C in a flow of nitrogen ($33.3 \text{ cm}^3 \text{ g}^{-1} \text{ s}^{-1}$) for 1 h at a ramping rate of 2 °C/min.

The commercial diesel oxidation catalyst (DOC) contains alumina-supported Pt, which is one of the most active elements for CO, C_3H_6 and NO oxidation [1,17]. A Pt/ Al_2O_3 model DOC catalyst was prepared for catalytic performance tests. Generally, $\gamma-Al_2O_3$ (Alfa Aesar) support powder was pretreated at 700 °C for 4 h in flowing dry air ($1.67 \text{ cm}^3 \text{ g}^{-1} \text{ s}^{-1}$) to prepare 2.0 wt% Pt/ Al_2O_3 by incipient wetness impregnation with $Pt(NH_3)_4(NO_3)_2$ (Sinopharm) precursor aqueous solution. The impregnated sample was dried at 120 °C overnight and treated in static air at 600 °C for 5 h. This preparation procedure led to the Pt/ Al_2O_3 catalyst having a surface area of 97.3 m^2/g and an average Pt particle size of 1.1 nm (as shown Fig. S1). The powder Pt/ Al_2O_3 model catalyst was pressed into pellets and sieved with mesh sizes of 180–250 μm , and reduced in a flow of 2.5% H_2/N_2 ($33.3 \text{ cm}^3 \text{ g}^{-1} \text{ s}^{-1}$) at 400 °C for 1 h at a ramping rate of 2 °C/min prior to the catalytic tests.

2.2. Catalytic reaction tests

Reactant gases (2% CO/N_2 , 1% NO/N_2 , 3% O_2/N_2 , 20% O_2/N_2 , 5% H_2/N_2 , high-purified N_2) were purchased from PurityPlus Specialty Gases. Reactant gas (1% C_3H_6/N_2) was obtained from Airgas, Inc. The gas flow rates were controlled and metered by mass flow controllers from MKS Instruments, Inc.

Light-off tests of carbon monoxide (CO) and propylene (C_3H_6) oxidation were carried out in a fixed-bed quartz tube reactor (4 mm inner diameter) with a ramp rate of 2 °C/min. The catalyst temperature was electronically controlled and measured by two K-type thermocouples located upstream and downstream of the catalyst bed. Since inlet and outlet temperatures were identical for all the runs, it can be assumed that the reactor was sufficiently controlled in an isothermal status. The catalysts (50 mg, 180–250 μm) were diluted with the same size silica gel (80 mg, Davisil Grade from Sigma Aldrich) that was pretreated at 800 °C for 4 h in static air prior to mixing. For typical CO only oxidation tests, a gas mixture containing 1% CO, 1.5% O_2 balanced with N_2 was fed into the reactor. For simulated diesel emissions of CO and C_3H_6 oxidation tests, a gas mixture containing 0.4% CO (when used), 0.1% C_3H_6 (when used), 0.05% NO (when used), 10% O_2 , and 5% H_2O (when used) with N_2 as balance was passed through the reactor. Deionized water was controlled and injected by a D-Series syringe pump from Teledyne Isco. To make liquid water fully vaporized, the main gas lines were wrapped by heating tapes and isolation materials to maintain the downstream lines isothermal at 120 °C up to the FTIR gas analyzer. The total flow rate for all the tests was fixed at 200 mL/min under standard temperature and pressure, corresponding to a weight hourly space velocity (WHSV) of 240, 000 $\text{mL g}^{-1} \text{ h}^{-1}$. An Antaris™ IGS Gas Analyzer from Thermo Fisher Scientific Inc. was used to analyze the gas reactants and products (CO, C_3H_6 , CO_2 , NO, NO_2 , N_2O , and H_2O). The conversion of CO, C_3H_6 , and NO to NO_2 are defined by the following equations, respectively.

$$X_{CO} = (C_{CO,in} - C_{CO,out}) / (C_{CO,in}) \times 100\% \quad (1)$$

$$X_{C_3H_6} = (C_{C_3H_6,in} - C_{C_3H_6,out}) / (C_{C_3H_6,in}) \times 100\% \quad (2)$$

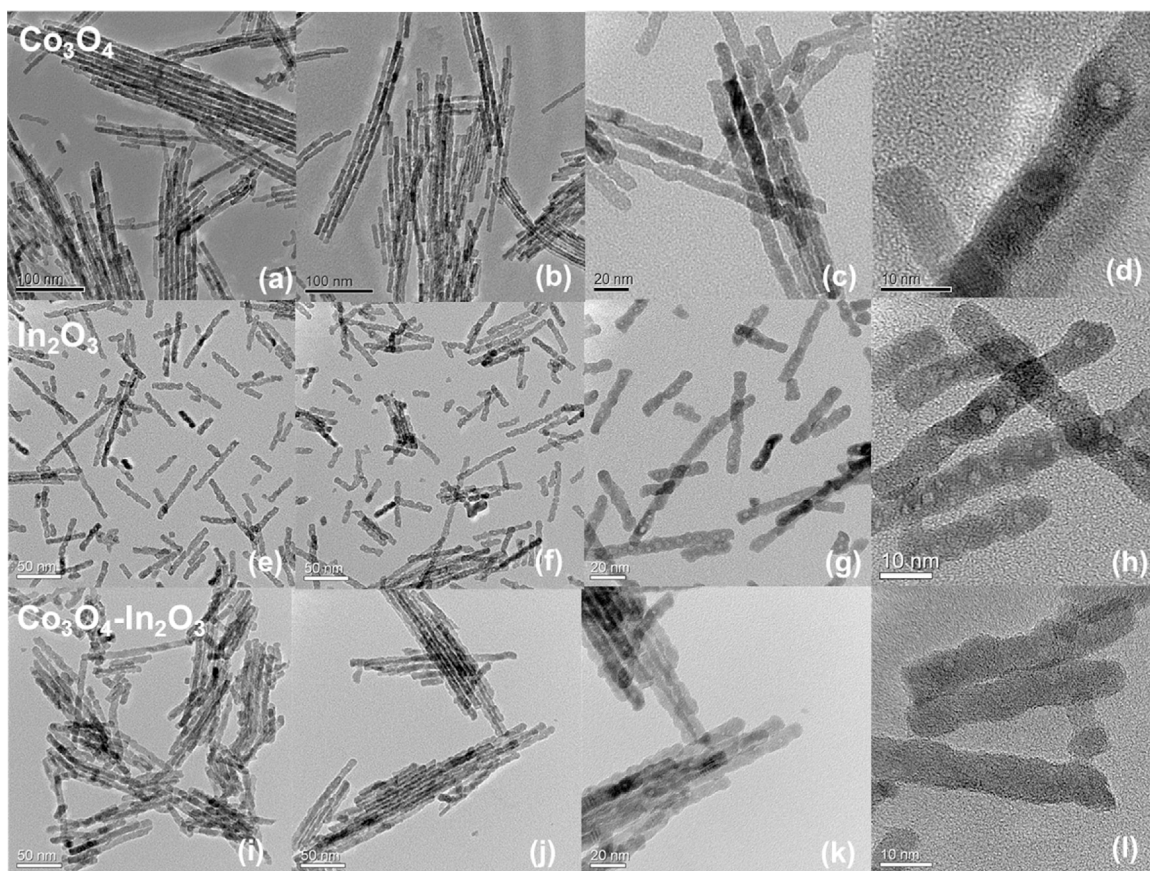


Fig. 1. TEM bright field images of (a–d) Co_3O_4 , (e–h) In_2O_3 , (i–l) $\text{Co}_3\text{O}_4\text{-In}_2\text{O}_3$ catalysts at different magnification scales.

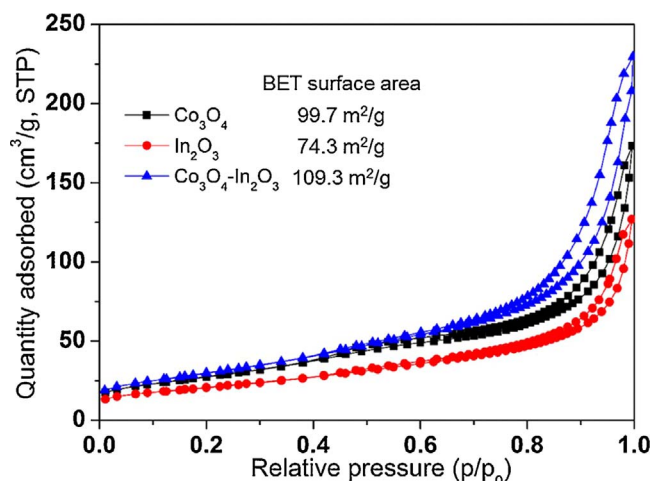


Fig. 2. N_2 adsorption-desorption isotherms of different catalysts.

$$X_{\text{NO-NO}_2} = (C_{\text{NO}_2, \text{out}} - C_{\text{NO}_2, \text{in}}) / (C_{\text{NO}, \text{in}}) \times 100\% \quad (3)$$

where $C_{\text{CO}, \text{in}}$, $C_{\text{CO}, \text{out}}$, $C_{\text{C}_3\text{H}_6, \text{in}}$, $C_{\text{C}_3\text{H}_6, \text{out}}$, $C_{\text{NO}, \text{in}}$, $C_{\text{NO}_2, \text{in}}$, and $C_{\text{NO}_2, \text{out}}$ represent the inlet and outlet gas concentrations.

2.3. Catalyst characterization

N_2 adsorption-desorption isotherms were carried out on a Micromeritics ASAP 2020 instrument using nitrogen gas as an adsorbate at 77 K. Before the tests, the samples were degassed under vacuum at 300 °C for 8 h. The Brunauer-Emmett-Teller (BET) equation was applied for the measurement of the specific surface area in the

relative pressure range of 0.05–0.35 (P/P_0). The pore size distribution of the SBA-15 template was determined by applying the Barrett-Joyner-Halenda (BJH) method for the data of nitrogen desorption branch.

Small-angle X-ray diffraction was carried out on a Rigaku Ultima IV instrument using $\text{Cu K}\alpha$ radiation ($\lambda = 1.54178 \text{ \AA}$) at 40 kV and 44 mA under ambient conditions. The scan angle extended from 0.02° to 8° using a step size of 0.02°, and accumulated data at a rate of 0.005°/s. Powder X-ray diffraction (XRD) measurements were carried out on a Rigaku rotary anode instrument using $\text{Cu K}\alpha$ radiation ($\lambda = 1.54178 \text{ \AA}$) at 40 kV and 100 mA under ambient conditions. The scan angle extended from 5° to 90° using a step size of 0.02°, and accumulated data at a rate of 0.033°/s. The observed data were analyzed by MDI Jade 2010 software. The structural parameters were analyzed by MAUD software of Rietveld refinement.

Transmission electron microscopy (TEM) images were taken on a JEOL 2010F analytical electron microscope with accelerating voltage of 200 kV. High-resolution transmission electron microscopy (HRTEM) and high-angle annular dark-field scanning transmission electron microscopy (HAADF-STEM) images were taken on a JEOL JEM3100R05 double Cs-corrected analytical electron microscope with accelerating voltage of 300 kV. Before the tests, small amounts of samples were diluted in ethanol and further dispersed by ultrasonication, and then dropped onto lacey formvar stabilized with carbon (200 mesh, copper grids) from Ted Pella, Inc.

X-ray photoelectron spectroscopy (XPS) experiments were carried out on a Kratos Axis Ultra XPS system at room temperature under $3.1 \times 10^{-8} \text{ Pa}$ using monochromatic Al source (14 kV and 8 mA). Binding energies of all the elements were calibrated relative to the adventitious carbon with C1s at 284.8 eV. All the data were analyzed by XPSPEAK software using Shirley type background.

Temperature-programmed reduction by H_2 ($\text{H}_2\text{-TPR}$) was performed on a ChemBET-3000 from Quantachrome Instruments. Typically,

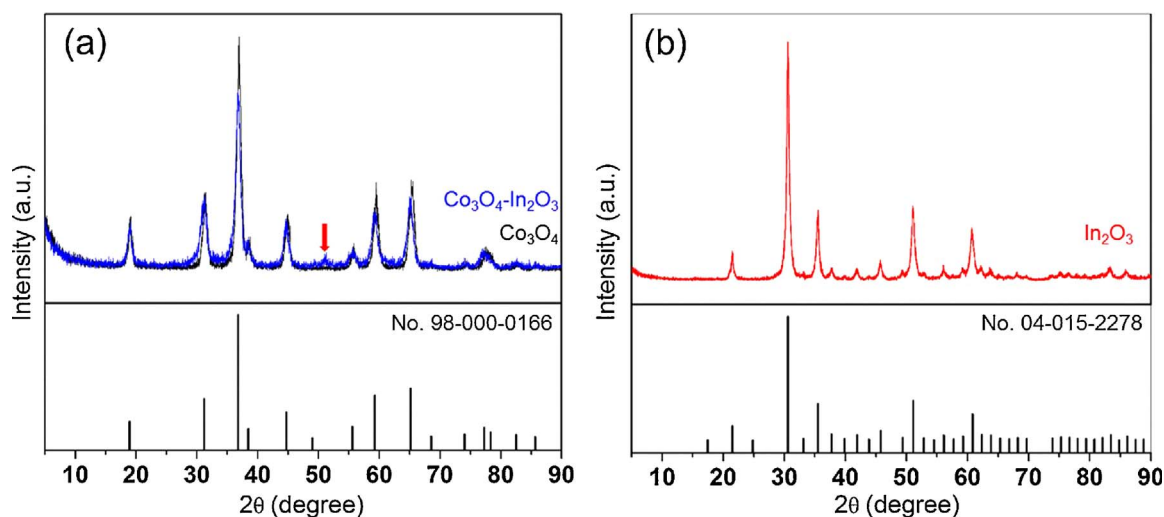


Fig. 3. XRD patterns of different catalysts.

4.4 mg sample was loaded in a U-type quartz reactor, and was pretreated in a flow of N_2 ($1.67 \text{ cm}^3 \text{ s}^{-1}$) at 300°C for 1 h to remove adsorbed water and other impurities. The sample was then cooled down to room temperature in a flow of nitrogen. After the baseline was stable when the current was set at 150 mA in a flow of 5% H_2/Ar ($1.17 \text{ cm}^3 \text{ s}^{-1}$), the sample was heated from room temperature with a ramp rate of $10^\circ\text{C}/\text{min}$. The signals of thermal conductivity detector (TCD) were qualitatively calibrated using high-purity CuO (Sigma Aldrich) with an assumption of stoichiometric reduction of CuO by H_2 . The qualitative results were analyzed by deconvolution of peaks using Origin Pro 2016 software. During the peak fitting process, all the sub-peaks were treated by Gaussian distribution with maximum numbers of iterations of 500, a tolerance of 1×10^{-15} , and adjusted R-squared higher than 0.9995.

Thermo-gravimetric (TG) analysis was performed on TA Q500 apparatus from TA instruments in a flow of N_2 ($1.67 \text{ cm}^3 \text{ s}^{-1}$) or 0.5% CO/N_2 ($1.67 \text{ cm}^3 \text{ s}^{-1}$) and the heating rate was $10^\circ\text{C}/\text{min}$ from 30 to 900°C . All the samples were pretreated in a flow of N_2 ($1.67 \text{ cm}^3 \text{ s}^{-1}$) at 300°C for 2 h before the tests.

In situ diffuse reflectance Fourier transform infrared spectroscopy (DRIFTS) experiments were conducted on a Bruker TENSOR 27 spectrometer equipped with an MCT detector cooled by liquid nitrogen. The catalyst was diluted with a 5% (w/w) ratio in KBr by mortar grinding, and then was loaded into the sample holder of a Praying Mantis™ High-Temperature Reaction Chamber with two ZnSe windows and a quartz window in the dome of the cell. Before the tests, the catalysts were pretreated in flowing nitrogen ($1.67 \text{ cm}^3 \text{ s}^{-1}$) at 300°C for 1 h, and then cooled to desired temperatures. At each temperature, the background spectrum was collected and subtracted from the sample spectrum at the same temperature.

3. Results and discussion

3.1. Characterizations of different nanorod catalysts

Textural and morphological properties of synthesized SBA-15 templates were characterized by XRD, N_2 physisorption and TEM techniques. As shown in Fig. S2, a very strong diffraction peak at 1.1° and two additional peaks at 1.8° and 2.0° were observed in small-angle XRD pattern, which could be indexed as (100), (110) and (200) reflections in hexagonal lattices, respectively [18]. A broad diffraction peak around 22.6° was observed in the wide-angle XRD pattern, and could be assigned to a typical peak of amorphous silica materials. N_2 adsorption-desorption isotherms showed a type IV isotherm with hysteresis loop of H1 type [19], further confirming the successful formation of the 2D-

hexagonal mesoporous structure of synthesized SBA-15 templates. The capillary condensation step in the relative pressure range of 0.6–0.8 implied a narrow distribution of relatively uniform pores. TEM images indicated the uniform mesoporous structure with a pore diameter of approximately 7.5 nm, which is similar to the value of 7.3 nm determined by pore size distributions from N_2 physisorption results.

The morphology of as-prepared different nanorods was investigated by transmission electron microscopy and shown in Fig. 1, and the fractional distributions of length and width were summarized in Fig. S3. Co_3O_4 samples exhibited uniform nanorod structures, and the width dimensions were approximately 6.7 nm in agreement with the pore size of the parent silica templates. In_2O_3 and $Co_3O_4-In_2O_3$ samples readily formed shorter nanorod structures most likely due to the relatively low diffusion coefficient of indium cations in the silica templates [20,21]. It should be noted that some regular circular holes were observed on the synthesized nanorods. It is believed that the formation of these circular holes can be attributed to the presence of silica plugs in the mesopores of the silica templates [22,23].

The textural and crystal structures of as-prepared different nanorods were characterized by N_2 physisorption and X-ray diffraction and shown in Figs. 2 and 3, respectively. Co_3O_4 , In_2O_3 , and $Co_3O_4-In_2O_3$ exhibited the BET surface areas of 99.7, 74.3 and $109.3 \text{ m}^2/\text{g}$, respectively. The diffraction peaks of $Co_3O_4-In_2O_3$ and Co_3O_4 perfectly matched each other having the crystal structure of pure Co_3O_4 spinel phase without any impurity phase, indicating a uniform distribution of indium cations in the entire cobalt oxide nanorod structure. The diffraction peaks of Co_3O_4 matched well with standard reference patterns of cubic Co_3O_4 (JCPDF No. 98-000-0166), suggesting the successful formation of Co_3O_4 spinel structure (space group $Fd\bar{3}m$ (227)). The diffraction peaks of In_2O_3 were consistent with standard reference patterns of cubic In_2O_3 (JCPDF No. 04-015-2278). Also, the diffraction peaks of $Co_3O_4-In_2O_3$ catalysts were almost the same as a pure Co_3O_4 catalyst, demonstrating excellent crystal phase purity in Co_3O_4 spinel structure with high indium doping level. Compared to Co_3O_4 catalysts, the locations of diffraction peaks slightly shifted to lower diffraction angles, indicating that In^{3+} could successfully substitute cobalt cations in Co_3O_4 lattices without causing any structural changes of the Co_3O_4 crystal structure. It should be noted that the formation of In_2O_3 could not be excluded, because a weak diffraction peak at 51.1° was observed on $Co_3O_4-In_2O_3$ catalysts that could be ascribed to diffraction peaks of the (440) plane in cubic In_2O_3 .

XPS was performed to probe the surface chemical states of different catalysts. The related fitting parameters and assignments are shown in Fig. 4 and tabulated in Table 1. For $Co_3O_4-In_2O_3$ catalysts, two major peaks with binding energies of Co $2p_{3/2}$ and Co $2p_{1/2}$ were 779.9 eV

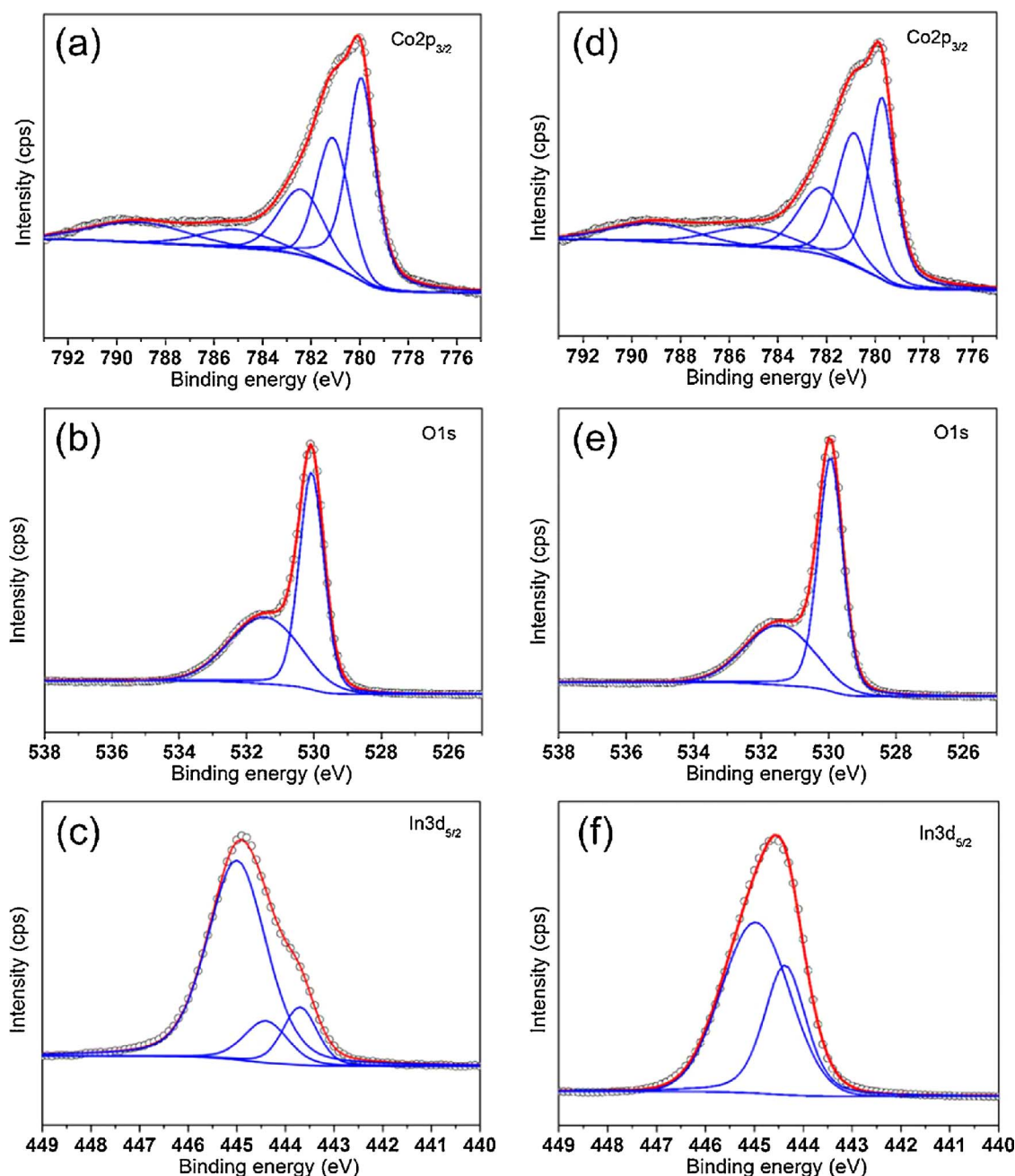


Fig. 4. Peak deconvolutions of Co $2p_{3/2}$, O $1s$ and In $3d_{5/2}$ core lines in X-ray photoelectron spectra for (a–c) $\text{Co}_3\text{O}_4\text{-In}_2\text{O}_3$, (d–e) Co_3O_4 , (f) In_2O_3 .

and 795.1 eV, respectively. The split spin-orbit of $2p$ is 15.2 eV characteristic Co_3O_4 phase. The high-resolution $\text{Co } 2p_{3/2}$ spectra could be fitted into three main peaks and two weak satellite shake-up peaks. The first peak at 779.9 eV could be assigned to both Co^{3+} and Co^{2+} , and the peaks at 781.1 eV and 782.4 eV could be assigned to Co^{3+} and Co^{2+} , respectively [24–27]. The peaks at higher binding energy of 785.1 eV and 789.1 eV are the satellite shake-up peaks of Co^{3+} and Co^{2+} [24–27]. As shown in Table 1, Co_3O_4 catalysts showed similar $\text{Co } 2p_{3/2}$ spectra without significant differences in comparison with $\text{Co}_3\text{O}_4\text{-In}_2\text{O}_3$ catalysts. Moreover, O $1s$ spectra of $\text{Co}_3\text{O}_4\text{-In}_2\text{O}_3$ catalysts are consistent with the spectra of stoichiometric Co_3O_4 catalysts. The O $1s$ region can be fitted with one main peak around 530.0 eV and one less intense peak around 531.5 eV, which could be assigned to lattice oxygen and surface or chemisorbed oxygen from Co_3O_4 spinels, respectively [28]. Obviously, the $\text{Co}_3\text{O}_4\text{-In}_2\text{O}_3$ sample exhibited a higher molar ratio of surface or chemisorbed oxygen (based on the relative

area in Table 1). The increased concentration of surface or chemisorbed oxygen would benefit the catalytic performance of cobalt oxide. For pure In_2O_3 nanorods, In $3d_{5/2}$ spectra could be fitted with two sub-peak components. The binding energy components at 445.0 eV and 444.4 eV were associated with the final states where the core holes were unscreened and screened, respectively [29,30]. The higher binding energy component was broader than the low binding energy component, and the energy separation between “unscreened” and “screened” final status is 0.6 eV, which is consistent with the reported results of In_2O_3 . It seems that the “unscreened” components played a role as the main components in $\text{Co}_3\text{O}_4\text{-In}_2\text{O}_3$ binary catalysts, yet the “screened” components significantly decreased and a small amount of indium metal formed when indium was doped into cobalt oxides [29–31].

The atom-resolved high angle annular dark-field (HAADF) and HRTEM images of $\text{Co}_3\text{O}_4\text{-In}_2\text{O}_3$ nanorods with distinct lattice fringes were further characterized by aberration-corrected electron microscopy

Table 1Binding energies, FWHM, and relative areas derived from curve deconvolutions of Co 2p_{3/2}, O 1s and In 3d_{5/2} spectra.

	Samples	Binding energies (eV)	FWHM (eV)	Relative area (%)	Assignment
Co 2p _{3/2}	Co ₃ O ₄ -In ₂ O ₃	779.9	1.37	38.5	Both Co ²⁺ and Co ³⁺
		781.1	1.60	24.1	Co ³⁺
		782.4	2.19	17.8	Co ²⁺
		785.1	3.55	7.9	Satellite shake-up peaks
		789.1	4.69	11.7	Satellite shake-up peaks
	Co ₃ O ₄	779.7	1.28	32.8	Both Co ²⁺ and Co ³⁺
		780.9	1.72	28.9	Co ³⁺
		782.2	2.29	19.2	Co ²⁺
		785.1	4.00	9.6	Satellite shake-up peaks
		789.1	4.11	9.6	Satellite shake-up peaks
O 1s	Co ₃ O ₄ -In ₂ O ₃	530.0	0.87	55.8	Lattice oxygen in spinel
		531.5	2.46	44.2	Surface or chemisorbed oxygen
	Co ₃ O ₄	529.9	0.86	61.1	Lattice oxygen in spinel
		531.5	2.40	38.9	Surface or chemisorbed oxygen
In 3d _{5/2}	Co ₃ O ₄ -In ₂ O ₃	445.0	1.43	75.9	Unscreened
		444.4	1.06	11.6	Screened
		443.7	0.83	12.5	Indium metal
	In ₂ O ₃	445.0	1.64	64.5	Unscreened
		444.4	1.01	35.5	Screened

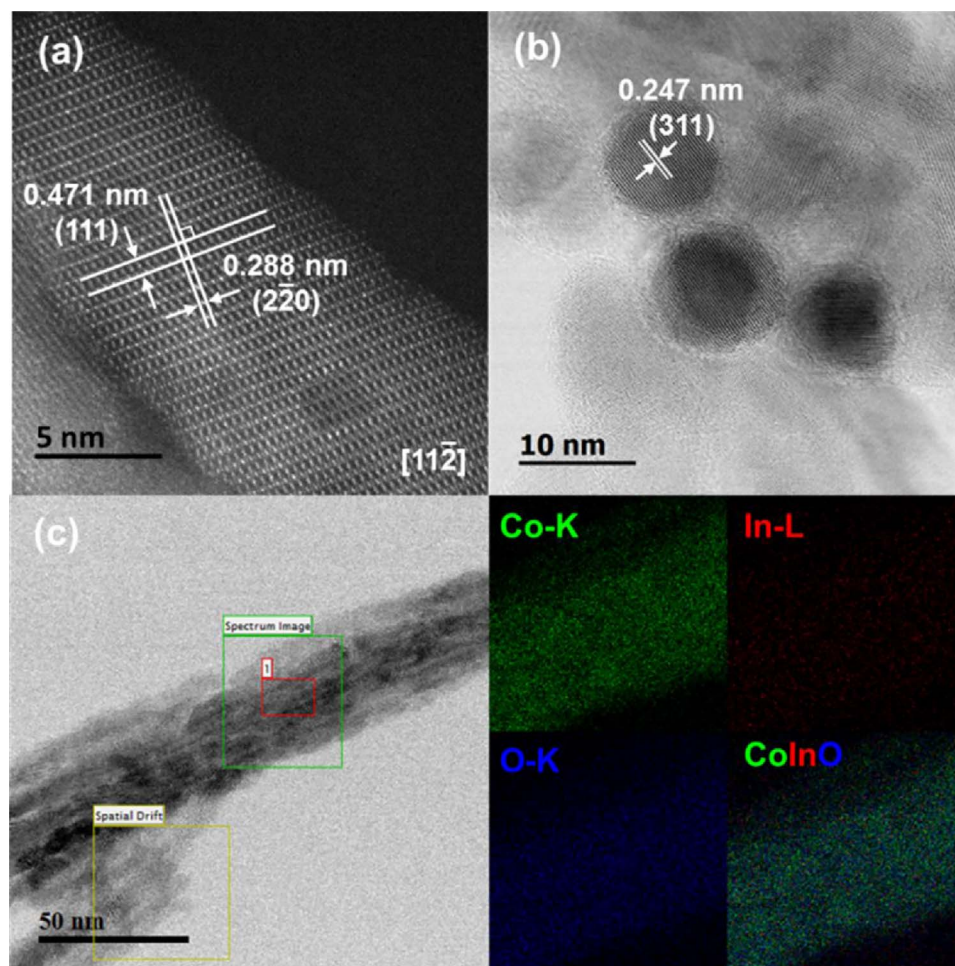


Fig. 5. High-resolution STEM HAADF and TEM images of Co₃O₄-In₂O₃ catalysts. (a) Main axis of nanorod perpendicular to the electron beam; (b) Main axis of nanorod parallel to the electron beam. (c) Co₃O₄-In₂O₃ nanorods and its micro-domain elemental mapping images by energy-dispersive X-ray spectroscopy.

and were shown in Fig. 5. The results illustrated that the surface of Co₃O₄-In₂O₃ nanorods could expose (220) lattice planes comprised of surface lattice oxygen coordinated with Co³⁺ sites that were active for CO oxidation [11]. The interplanar d-spacing of 0.288 nm and 0.471 nm with an interfacial angle of 90° could be assigned to the lattice planes of (220) and (111) of cobalt oxide crystals, suggesting that the crystal was viewed along the [112] directions. It should be noted

that the d-spacing value is slightly larger than the standard value of 0.28581 nm and 0.46673 nm for (220) and (111) of Co₃O₄ (JCPDF No. 98-000-0166), indicating that the doping with large indium ions caused lattice expansion. The speculation of lattice expansion could also be evidenced by the slight difference of cell parameters resolved by Rietveld refinement in Table 2. In addition, energy dispersive X-ray spectroscopy (EDS) characterization was carried out to determine the

Table 2
Elemental compositions and Rietveld refinement results of $\text{Co}_3\text{O}_4\text{-In}_2\text{O}_3$ and Co_3O_4 catalysts.

Samples	Elemental compositions			Elemental compositions			Elemental compositions		a (Å)	R _{wp} (%)
	XPS (wt%)			EDS (wt%)			ICP-OES (wt%)			
	Co	In	O	Co	In	O	Co	In		
Co ₃ O ₄ -In ₂ O ₃	61.1	14.2	24.7	60.9	10.4	28.7	55.5	12.0	8.10	11.5
Co ₃ O ₄	–	–	–	–	–	–	–	–	8.07	13.3

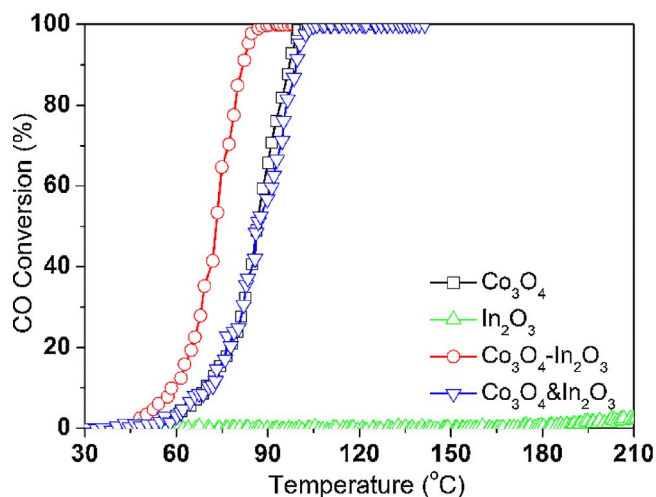


Fig. 6. Light-off curves of CO oxidation over $\text{Co}_3\text{O}_4\text{-In}_2\text{O}_3$, Co_3O_4 , In_2O_3 , and $\text{Co}_3\text{O}_4 \& \text{In}_2\text{O}_3$ catalysts. $\text{Co}_3\text{O}_4\text{-In}_2\text{O}_3$ stands for indium-promoted Co_3O_4 nanorods, and $\text{Co}_3\text{O}_4 \& \text{In}_2\text{O}_3$ stands for physical mixtures of Co_3O_4 and In_2O_3 nanorods. Reaction condition: 1% CO, 1.5% O_2 balanced with N_2 at WHSV = 240, 000 $\text{mL g}^{-1} \text{h}^{-1}$.

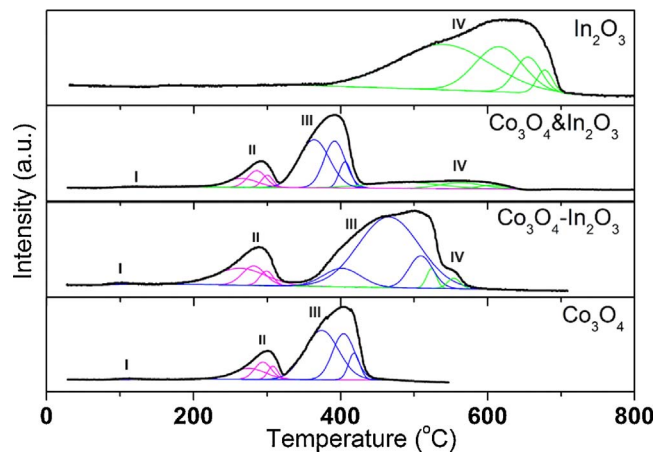


Fig. 7. H_2 -TPR profiles of different catalysts.

distribution of indium cations in $\text{Co}_3\text{O}_4\text{-In}_2\text{O}_3$ nanorods. The elemental mapping results indicated that both cobalt and indium elements were uniformly dispersed over the entire $\text{Co}_3\text{O}_4\text{-In}_2\text{O}_3$ nanorod structures with In^{3+} substituting cobalt cations in Co_3O_4 lattice.

As shown in Fig. S4, the elemental compositions of Co, In and O in $\text{Co}_3\text{O}_4\text{-In}_2\text{O}_3$ nanorod catalysts were analyzed and tabulated in Table 2. EDS clearly detected the existence of indium cations in $\text{Co}_3\text{O}_4\text{-In}_2\text{O}_3$ catalysts without any other significant impurity phase. The quantitative results of different elementals were almost consistent with the surface results detected by XPS and also ICP-OES techniques. It should be noted that copper signals stemmed from the copper grids. Trace amounts of Si (< 0.50 wt%) was also detected, indicating that the silica template could be removed down to trace levels during the etching process.

These trace amounts of Si were not considered in the total elemental composition calculations.

3.2. Synergistic roles in indium-doped Co_3O_4 catalysts

The catalytic activities of as-prepared different catalysts were initially evaluated by catalytic oxidation of CO. As shown in Fig. 6, almost no CO oxidation activity was observed over In_2O_3 nanorods within the test temperature range. The catalytic performance of $\text{Co}_3\text{O}_4\text{-In}_2\text{O}_3$ nanorods was much higher than Co_3O_4 and $\text{Co}_3\text{O}_4 \& \text{In}_2\text{O}_3$. The enhanced catalytic performance over $\text{Co}_3\text{O}_4\text{-In}_2\text{O}_3$ nanorods could be attributed to the strong synergistic roles between cobalt and indium cations. Evidence for this interaction is provided by comparing the reducibility of different catalysts in the following temperature-programmed results including TPR and TGA characterizations. The results confirmed that lattice oxygen could be much more easily abstracted by hydrogen from indium-doped Co_3O_4 than from Co_3O_4 and the physical mixture $\text{Co}_3\text{O}_4 \& \text{In}_2\text{O}_3$. The presence of indium with its large cation radius might influence the chemical status of surface/chemisorbed oxygen in $\text{Co}_3\text{O}_4\text{-In}_2\text{O}_3$ nanorods, thereby increasing the mobility of lattice oxygen involved in the catalytic oxidation reaction.

H_2 -TPR techniques are used to confirm the reducibility of as-prepared catalysts. Distinct reduction curves are observed for each catalyst as shown in Fig. 7, and the detailed quantitative results of different peaks are summarized in Table 3. For pure Co_3O_4 , there were three well-resolved reduction peaks observed. The first weak peak centered at 111°C could be assigned to very active surface oxygen species [32,33]. The two reduction peaks at higher temperatures could be assigned to the stepwise reduction of Co_3O_4 to metallic cobalt. Accordingly, the second reduction peak around 294°C should be the reduction of Co_3O_4 to CoO ($\text{Co}_3\text{O}_4 + \text{H}_2 \rightarrow 3\text{CoO} + \text{H}_2\text{O}$), and the third reduction peak around 404°C should be the reduction of CoO to metallic cobalt ($3\text{CoO} + 3\text{H}_2 \rightarrow 3\text{Co} + 3\text{H}_2\text{O}$) [33–35]. As shown in Table 3, the peak area ratio of peak(III)/peak(II) is about 3.8, slightly higher than the theoretical value of 3.0, while the total hydrogen consumption of Co_3O_4 accounted for approximately 89% of the theoretical amount. This probably implies that only parts of Co^{3+} could be reduced during this reduction process. For the case of In_2O_3 reduction, one broad reduction peak around 616°C was observed, which could be assigned to the reduction process of In_2O_3 to metallic indium. The actual hydrogen consumption of In_2O_3 reduction was $11.0 \text{ mmol/g}_{\text{cat}}$, very close to the theoretical value of hydrogen consumption of $10.8 \text{ mmol/g}_{\text{cat}}$, indicating that In_2O_3 nanorods could be completely reduced during this reduction process. For $\text{Co}_3\text{O}_4\text{-In}_2\text{O}_3$ catalysts, the reduction peaks of active surface oxygen (peak I) and Co^{3+} reduction (peak II) shifted to lower temperatures at 101°C and 282°C , respectively. The shift of these reduction peaks is generally recognized as a sign of the improved reducibility of Co^{3+} to Co^{2+} caused by doping with indium. In comparison with the reduction profiles of both Co_3O_4 and In_2O_3 , the Co^{2+} reduction peak (peak III) shifted to a higher temperature around 466°C , while the In^{3+} reduction peak (peak IV) shifted to a lower temperature around 554°C . Since Co^{2+} would be reduced to Co^0 during the peak III process, it appears that the spillover of hydrogen from metallic cobalt to In_2O_3 might facilitate the reduction process of In^{3+} . The shifts of peak III and IV locations further indicated the presence of strong interactions

Table 3
Quantitative results of hydrogen consumption and peak area in H₂-TPR profiles.

Samples	Gaussian sub-peaks			Peak area ratio of III/II	Total hydrogen consumption (mmol/g _{cat})				
	Peak No.	Center (°C)	Peak Area		Actual	Theoretical			
Co ₃ O ₄	I	111	31.8	3.8	14.8	16.6			
		275	547.8						
	294	439.9							
	308	198.9							
	374	2552.3							
Co ₃ O ₄ -In ₂ O ₃ ^a	III	404	1553.0	3.9	13.6	14.1			
		418	455.8						
		101	22.2						
	II	263	572.2				3.8	15.4	15.1
		282	297.1						
299		129.1							
Co ₃ O ₄ & In ₂ O ₃ ^b	III	402	460.6	3.8	15.4	15.1			
		466	2878.3						
		509	512.7						
	IV	524	129.9				–	11.0	10.8
		554	87.9						
I		120	32.7						
In ₂ O ₃	II	265	399.3	–	11.0	10.8			
		286	432.4						
		300	197.6						
	III	364	2104.6				–	11.0	10.8
		392	1405.2						
		406	433.0						
	IV	487	624.3	–	11.0	10.8			
		564	373.6						
		606	138.3						
	IV	540	1933.2				–	11.0	10.8
616		978.8							
655		424.0							
678		163.6							

^a Theoretical hydrogen consumption of Co₃O₄-In₂O₃ catalyst was calculated based on ICP-OES results.

^b Co₃O₄ & In₂O₃ catalyst loading for H₂-TPR tests was 5.0 mg, with 26% weight percent of In₂O₃, while all the other catalysts had a loading of 4.4 mg.

between cobalt and indium. For better understanding of this strong interaction, the reducibility of physical mixtures of Co₃O₄ and In₂O₃ (Co₃O₄ & In₂O₃) catalysts were also tested. For this case, the reduction peaks included the first three reduction peaks of stepwise reduction of Co₃O₄ to metallic cobalt and the fourth reduction peak of In₂O₃. There were no significant location changes for all these four reduction peaks in comparison with both Co₃O₄ and In₂O₃ catalysts, suggesting the absence of strong interactions between cobalt and indium, and highlighting that proximities of cobalt and indium species would greatly matter for the interactions.

As shown in Fig. 8(a), the total weight loss for Co₃O₄ and Co₃O₄-In₂O₃ catalysts was 8.1 wt% and 6.9 wt% in the presence of nitrogen, respectively. Generally, the weight loss below 700 °C is considered to result from desorption of surface adsorbed OH and nonstoichiometric oxygen [36–38]. The major weight loss for Co₃O₄ catalysts, taking place above 700 °C, was approximately 6.1 wt%. Because this weight loss amount was in good agreement with the stoichiometry of Co₃O₄ decompositions (Co₃O₄ → 3CoO + 1/2O₂), it can be attributed to the lattice oxygen loss from Co₃O₄ [37,38]. Meanwhile, the weight loss above 700 °C on Co₃O₄-In₂O₃ catalysts was 5.2 wt%, and could also be attributed to lattice oxygen loss from Co₃O₄, since indium oxides were relatively stable and did not show any significant weight loss during the thermal treatment in a nitrogen atmosphere. The weight loss curves could be further transformed into intense peaks in derivative plots (DTG) that are displayed in Fig. 8(b). The peak onset for Co₃O₄-In₂O₃ catalysts slightly shifted to lower temperatures in comparison with Co₃O₄ catalysts in the DTG curves, implying the improved ability to abstract lattice oxygen by doping indium into cobalt oxides. Since surface lattice oxygen coordinated with Co³⁺ was usually considered as the active species in CO oxidation [11], TG analysis in CO atmosphere was also carried out to titrate active lattice oxygen from bulk catalysts. As shown in Fig. 8(c), the first significant weight loss of both Co₃O₄-

In₂O₃ and Co₃O₄ catalysts was observed around 240 °C. This weight loss stage indicated that the active surface lattice oxygen was gradually consumed by the CO in the gas phase. Fig. 8(d) showed that the first maximum weight loss rate over Co₃O₄-In₂O₃ centered at 288 °C, lower than Co₃O₄ catalysts centered at 301 °C. The result further demonstrated that the indium doping greatly enhanced the activation of lattice oxygen involved in CO oxidation. Furthermore, In₂O₃ was relatively stable in the presence of CO, and the maximum weight loss rate was observed around 333 °C. This result implied that In₂O₃ was not active for CO oxidation during this heating process, which could also be confirmed by the CO catalytic oxidation tests.

3.3. Catalytic performance in simulated diesel exhaust

Fig. 9 shows CO, C₃H₆ and NO oxidation activities for comparison of Co₃O₄-In₂O₃ nanorods and Pt/Al₂O₃ catalysts in simulated diesel exhaust. For gaining meaningful comparisons with literature results, this simulated diesel exhaust condition was selected to be similar to DOCs test conditions for Co-Cu-Ce [10] and Pd/SiO₂ [39] catalysts. Under this test condition, Co₃O₄-In₂O₃ nanorod catalysts significantly outperformed the Pt/Al₂O₃ catalysts in CO oxidation, while giving similar C₃H₆ and NO oxidation performance. Remarkably, during long-term stability tests under full exhaust mixture, no significant activity loss for CO and C₃H₆ oxidation was observed, and the Co₃O₄-In₂O₃ catalysts could still maintain their uniform nanorod structures (as shown in Fig. 10). For further examining the hydrothermal stability of Co₃O₄-In₂O₃ catalysts, both Co₃O₄-In₂O₃ and Pt/Al₂O₃ catalysts were hydrothermally treated in flowing of 10% H₂O/Air at 750 °C for 120 min. As shown in Fig. S5, Co₃O₄-In₂O₃ catalysts could still outperform Pt/Al₂O₃ in CO oxidation, but exhibited a performance loss for C₃H₆ and NO oxidation. The performance loss should be ascribed to the morphology change during the harsh pretreatment condition, while the aged sample

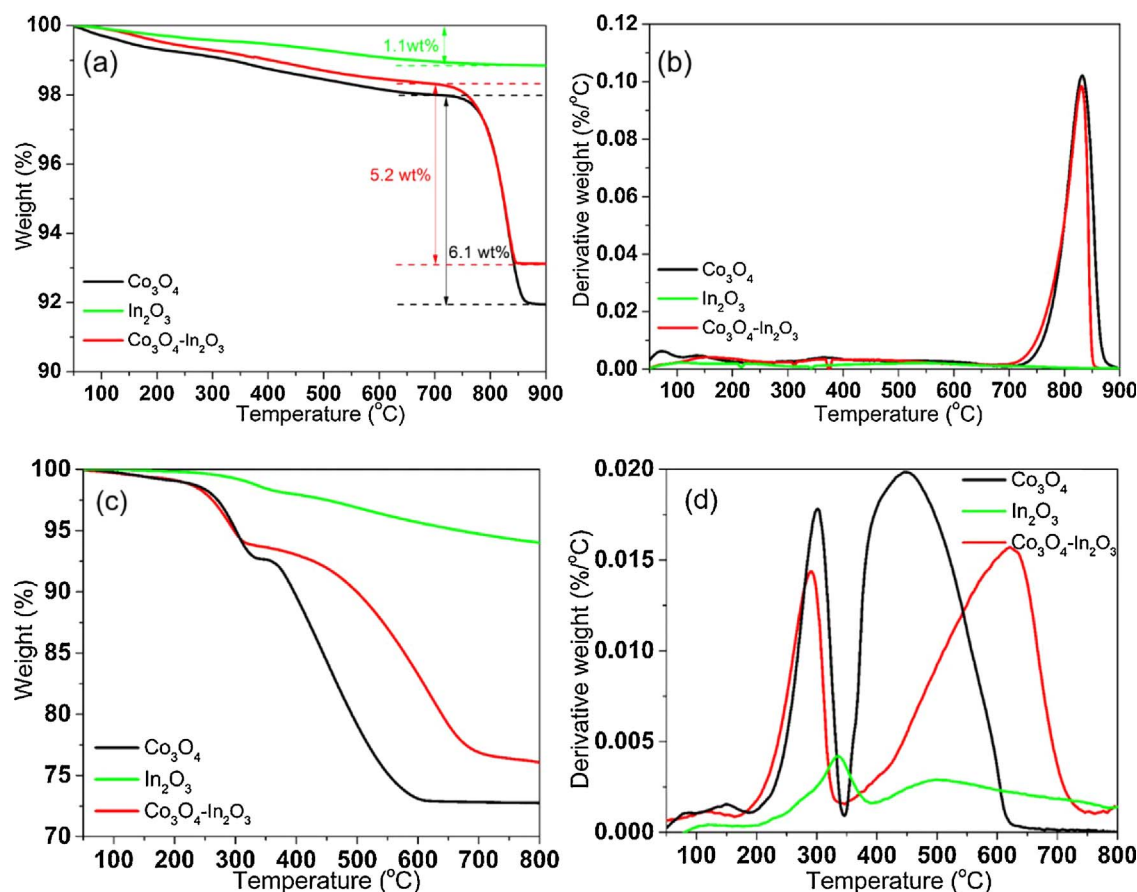


Fig. 8. Thermo-gravimetric analysis and derivative thermogravimetry (DTG) curves of different catalysts during thermal treatment in nitrogen (a–b) and in 0.5% CO/N₂ (c–d).

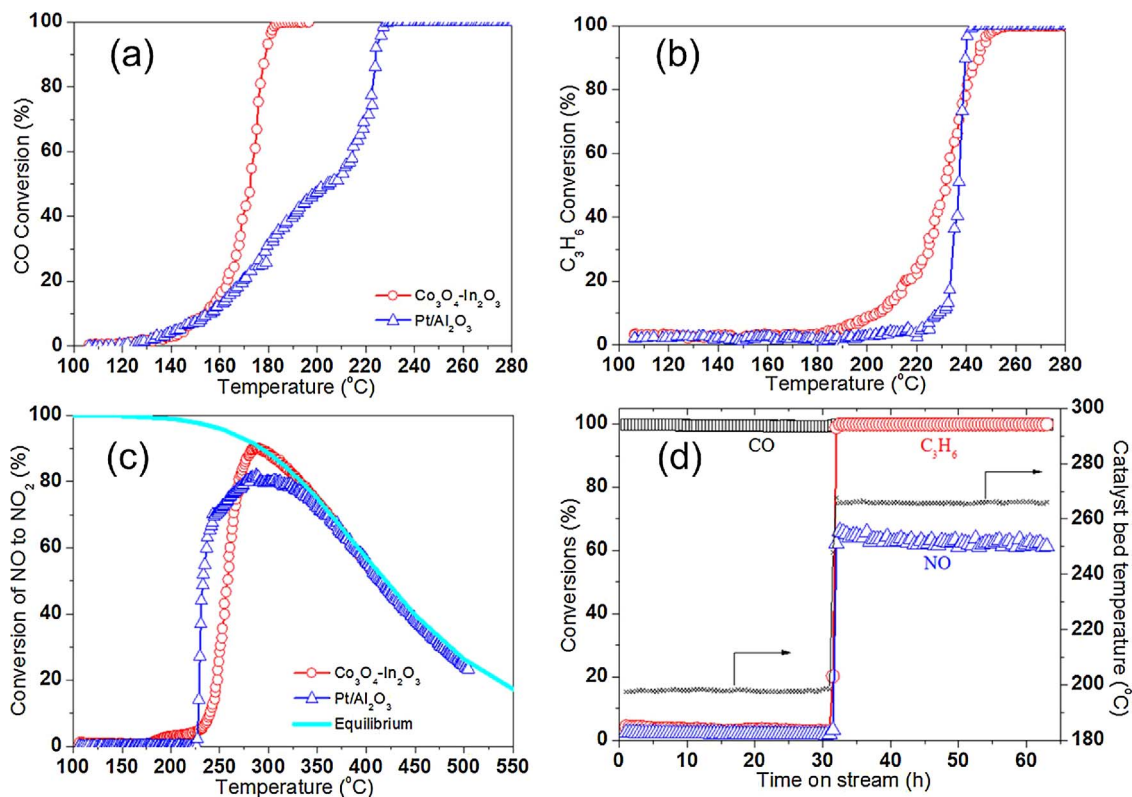


Fig. 9. Catalytic oxidation of CO, C₃H₆, and NO on Co₃O₄-In₂O₃ and Pt/Al₂O₃ catalysts. (a) Light-off curves of CO. (b) Light-off curves of C₃H₆. (c) Conversions of NO to NO₂. Equilibrium conversion curves were calculated based on the thermodynamics where [NO] = 500 ppm and [O₂] = 10%. (d) Long-term stability tests of fresh Co₃O₄-In₂O₃ catalysts. Reaction condition: 0.4% CO, 0.1% C₃H₆, 0.05% NO, 10% O₂, 5% H₂O balanced with N₂ at WHSV = 240, 000 mL g⁻¹ h⁻¹.

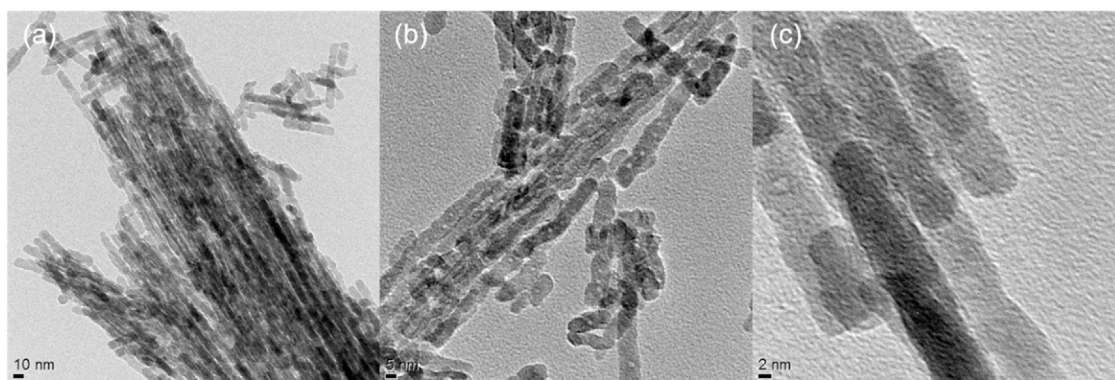


Fig. 10. (a–c) TEM bright field images of $\text{Co}_3\text{O}_4\text{-In}_2\text{O}_3$ catalysts after long-term stability tests viewed at different magnification scales.

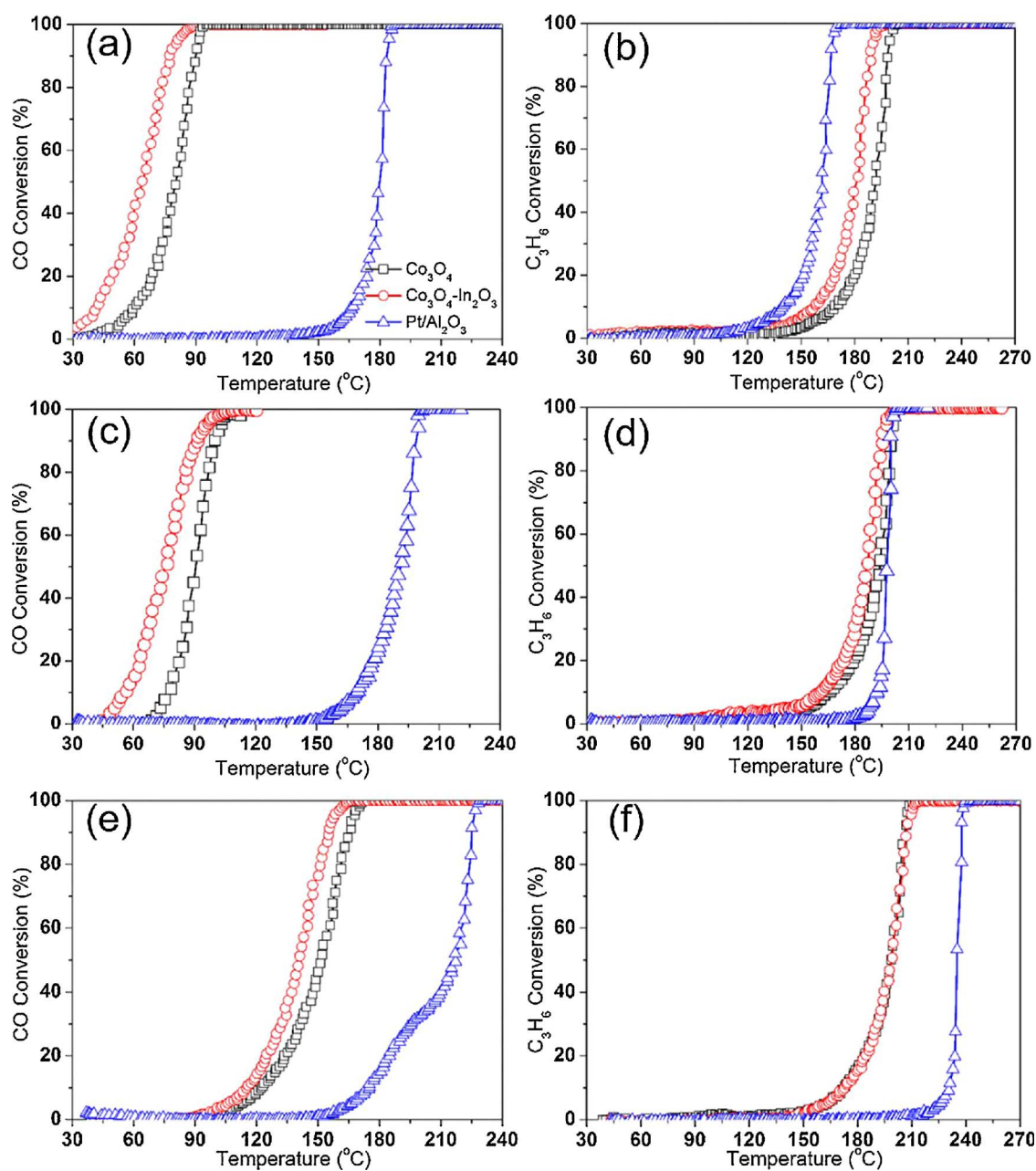


Fig. 11. Light-off curves of CO (a, c, e) and C_3H_6 (b, d, f) oxidation over $\text{Co}_3\text{O}_4\text{-In}_2\text{O}_3$ and Co_3O_4 , and $\text{Pt}/\text{Al}_2\text{O}_3$ catalysts. Reaction conditions: (a) 0.4% CO, 10% O_2 balanced with N_2 ; (b) 0.1% C_3H_6 , 10% O_2 balanced with N_2 ; (c–d) 0.4% CO, 0.1% C_3H_6 , 10% O_2 balanced with N_2 ; (e–f) 0.4% CO, 0.1% C_3H_6 , 0.05% NO , 10% O_2 balanced with N_2 . All the reactions were kept at $\text{WHSV} = 240,000 \text{ mL g}^{-1} \text{ h}^{-1}$.

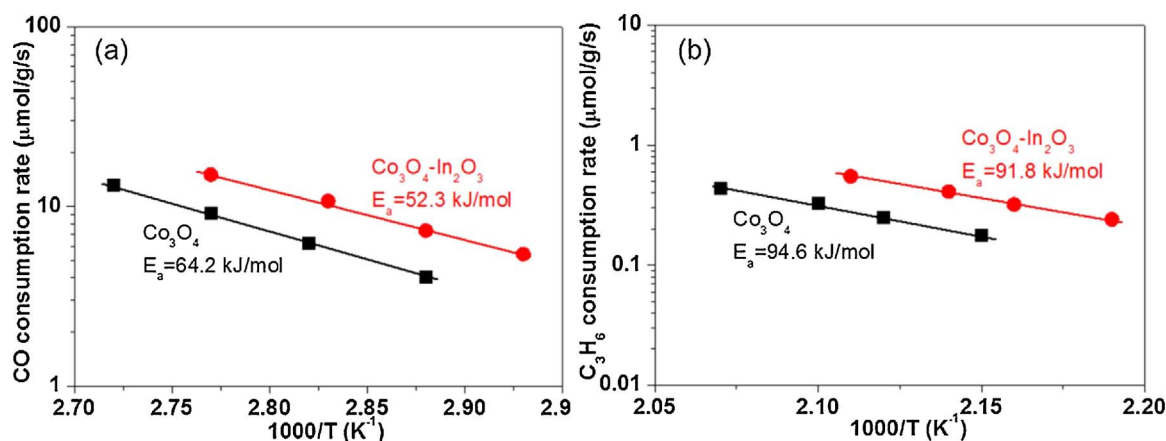


Fig. 12. Arrhenius plots of (a) CO and (b) C₃H₆ oxidation on Co₃O₄-In₂O₃ and Co₃O₄ catalysts.

could still maintain the good crystal structure of Co₃O₄ spinel phase (Fig. S6). For comparison of catalytic activities, reaction temperatures of T₅₀ and T₉₀ were used corresponding to catalytic conversions of 50% and 90%, respectively. T₅₀ and T₉₀ values of Co₃O₄-In₂O₃ along with literature results of commercial DOC, Pt/Al₂O₃ model catalysts, and Pt-Pd/Al₂O₃ model catalysts are summarized in Table S1. The results show that the Co₃O₄-In₂O₃ nanorods exhibited much better catalytic performance in CO oxidation and comparable C₃H₆ oxidation ability. Of course, while the nanorod catalyst is very promising, it still remains to be explored how it can be placed on a washcoated monolith and how it performs in tests following the CLEERS protocols of diesel emissions, where the catalysts get exposed to simulated drive cycles with full gas mixtures.

Light-off experiments of CO and C₃H₆ oxidation in different atmospheres were also carried out to understand the different roles of CO, C₃H₆, and NO in simulated diesel reactions. As shown in Fig. 11, the light-off temperatures of CO oxidation on Co₃O₄-In₂O₃ and Co₃O₄ catalysts were not significantly influenced by the presence of C₃H₆ (Fig. 11(a) and (c)). And, the presence of CO also did not significantly influence light-off temperatures of C₃H₆ oxidation (Fig. 11(b) and (d)). The above results suggested that there was no significant interference between CO and C₃H₆ gases over Co₃O₄-In₂O₃ and Co₃O₄ nanorod catalysts, in stark contrast to Pt-based catalysts where C₃H₆ shifts the CO light-off temperature to much higher temperatures (3). However, the presence of NO did shift the light-off curves to higher temperatures, indicating that NO could strongly inhibit the oxidation of CO and C₃H₆ (Fig. 11(e) and (f)). This result was consistent with the study that showed that NO could be the main inhibitor of catalytic oxidation reactions, most likely related to the formation of nitrate species on the catalyst surface by competitive adsorption [40]. As shown in Fig. S7, FTIR study of co-adsorption of NO, CO, and C₃H₆ further confirmed this speculation, while carbonates (1394 and 1368 cm⁻¹) accompanied with some amount of nitrates (1611 cm⁻¹) [41] were formed at the surface of Co₃O₄-In₂O₃ catalysts at different reaction temperatures. The Arrhenius plots for CO and C₃H₆ oxidation, and the apparent activation energies (E_a) obtained over the Co₃O₄-In₂O₃ and Co₃O₄ nanorod catalysts are shown in Fig. 12. The E_a values for CO oxidation were 52.3 and 64.2 kJ/mol for Co₃O₄-In₂O₃ and Co₃O₄ catalysts, respectively, while the apparent activation energies for C₃H₆ oxidation were 91.8 and 94.6 kJ/mol, respectively. The lower E_a values indicated catalytic oxidation reactions took place much easier over indium doped Co₃O₄ catalysts.

3.4. The reaction mechanism study by FTIR and kinetics

Infrared spectroscopy of adsorbed molecules was carried out to understand the detailed reaction mechanism of CO and C₃H₆ oxidation

over Co₃O₄-In₂O₃ catalysts. Fig. 13(a) shows the FTIR spectra of CO adsorption on Co₃O₄-In₂O₃ catalysts. The spectra mainly contain two weak bands at 2168 and 2111 cm⁻¹ and three intense bands at 1536, 1386, and 1315 cm⁻¹ at 65 °C. The two weak bands could be assigned to gaseous CO adsorbed on the catalyst surface [42,43], since these species could be easily removed by nitrogen purging. Also, the intense peaks at 1536 and 1315 could be assigned to νC=O and ν_{as}COO of bidentate carbonates, respectively, while the peak at 1386 cm⁻¹ could be assigned to monodentate carbonates [43–46]. The formation of different carbonates indicated that the adsorbed CO could readily react with active oxygen from Co₃O₄-In₂O₃ catalysts to generate carbonates. These kinds of carbonates should be relatively stable, since their intensities did not obviously change during the following N₂ or O₂ purging. As shown in Fig. 13(b), two strong peaks at 1537 and 1308 cm⁻¹ were observed at 30 °C for CO and O₂ co-adsorption on Co₃O₄-In₂O₃ catalysts, which could also be assigned to vibrations of bidentate carbonates. Obviously, the intensities of these two peaks gradually increased as temperatures went up, indicating that the reactions of bidentate carbonate formation would be facilitated with increasing temperature. The slight change of band positions from 1400 cm⁻¹ to 1378 cm⁻¹ might imply the reaction between CO and active oxygen. It appears that the Co₃O₄-In₂O₃ catalyst was very active for the formation of bidentate carbonates, which could act as reaction intermediates and further oxidize CO into CO₂ also evidenced by the kinetic results [43]. Fig. 13(c) shows the FTIR spectra of C₃H₆ adsorption on Co₃O₄-In₂O₃ catalysts. At room temperature, an intense IR band at 1637 cm⁻¹ was observed and assigned to the characteristic band of C=C stretching of propylene, and less intense IR bands at 1427 and 1365 cm⁻¹ due to asymmetric and symmetric deformation of C–H from formate species [47–50]. With temperature increasing to 190 °C, the intensity of the C=C stretching band significantly decreased, but the intensities of the C–H band deformation increased. It meant that C₃H₆ would be activated by the active oxygen from cobalt oxides to form abundant formate species, which could further be oxidized by oxygen into final products of CO₂ and water. As shown in Fig. 13(d), the assignment of formate formation could also be confirmed by steady state adsorption of C₃H₆ and O₂ at high temperatures. The formate peaks at 1427 and 1364 cm⁻¹ were observed at 140 and 190 °C, but the intensities gradually decreased with increasing temperatures. This behavior might indicate that formate was not stable, and would decompose according to “HCO₂⁻ → CO + OH⁻” at high temperatures [50]. At temperatures above 210 °C, formation of acetate (bands at 1593, and 1486 cm⁻¹) and acetone (band at 1674 cm⁻¹) was observed [47–50]. These species were proposed as the reaction intermediates generated from formate during total oxidation of propylene over cobalt oxides [50,51]. In the catalytic performance results, Co₃O₄-In₂O₃ nanorod catalysts started combustion activity around 120 °C, while the formate species could be

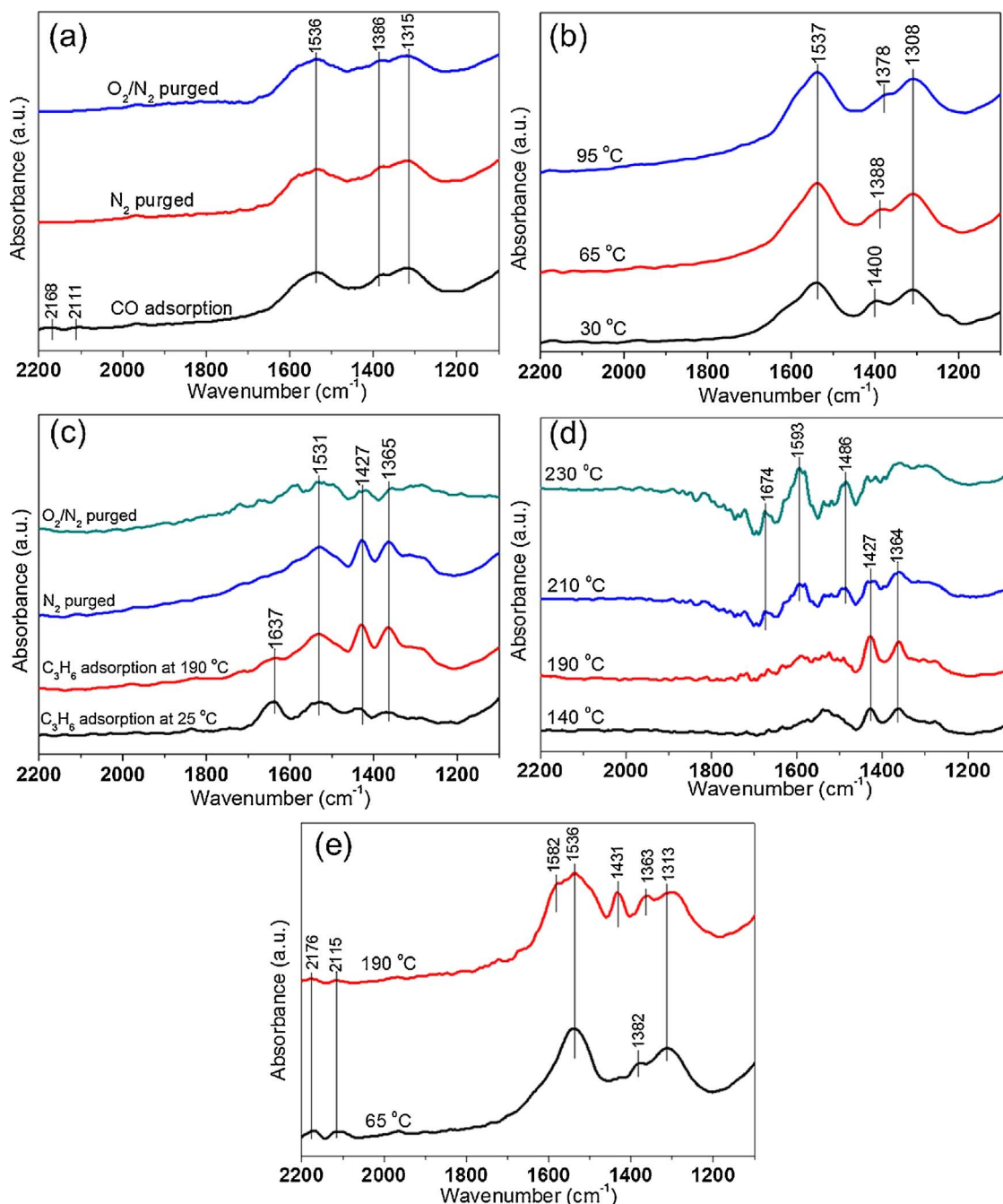


Fig. 13. *In situ* FTIR spectra on Co₃O₄-In₂O₃ catalysts of (a) CO adsorbed at 65 °C followed by N₂ purging and O₂/N₂ reaction. (b) CO and O₂ co-adsorption at various temperatures. (c) C₃H₆ initially adsorbed at 25 °C and then adsorbed at 190 °C followed by N₂ purging and O₂/N₂ reaction. (d) C₃H₆ and O₂ co-adsorption at various temperatures. (e) CO, C₃H₆ and O₂ co-adsorption at 65 °C and 190 °C, respectively.

significantly consumed by oxygen in the following oxygen purging process. Therefore, it is reasonable to infer that the formate species should be reaction intermediates for propylene oxidation on as-prepared Co₃O₄-In₂O₃ nanorod catalysts before the formation of CO₂ and water. Fig. 13(e) shows the coadsorption of CO and C₃H₆ on Co₃O₄-In₂O₃ at 65 °C and 190 °C. Only bidentate carbonates (1536 and 1313 cm⁻¹), monodentate carbonates (1382 cm⁻¹) and gaseous CO (bands at 2176 and 2115 cm⁻¹) were observed at 65 °C. After the reaction temperature increased to 190 °C, the intense adsorption bands of formates (1536 and 1313 cm⁻¹) and acetates (1582 cm⁻¹) would appear without any significant change of surface carbonates.

Before conducting kinetic measurement, heat and mass transfer limitations have been ruled out based on the experimental and also

theoretical evidence. As shown in Fig. S8, the effects of intraparticle or interparticle SiO₂/catalyst dilution ratios on CO/C₃H₆ oxidation consumption rate have been carried out. The results showed that CO/C₃H₆ oxidation consumption rate did not depend on intraparticle or interparticle dilution ratios, indicating that the local concentrations and temperatures were identical with that measured in the fluid phase. Also, Table S2 and related discussions indicated that there were no obvious heat and mass transfer limitations in the catalytic tests for Co₃O₄-In₂O₃ catalysts. Since all the other catalysts were evaluated under similar reaction conditions, it could be assumed that there should be no obvious heat and mass transfer limitations in all the catalytic tests. For kinetic measurement, a differential reactor was assumed, since the maximum CO/C₃H₆ conversions were around 18%, and most

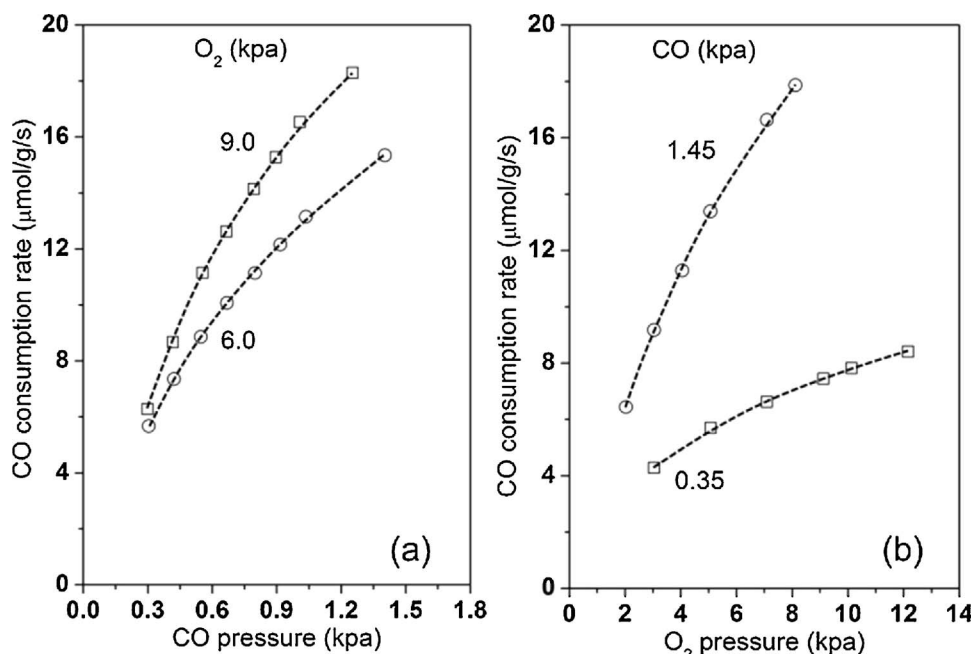
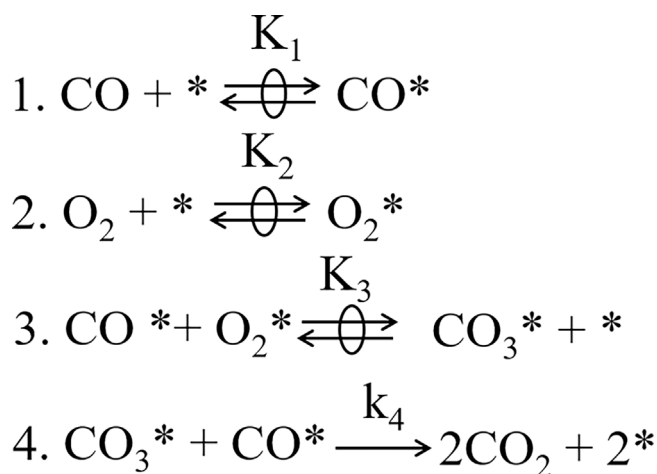


Fig. 14. Effects of CO (a) and O₂ (b) pressures on CO consumption rate on Co₃O₄-In₂O₃ nanorod catalysts at 358 K.



Scheme 1. The elementary step of CO catalytic oxidation.

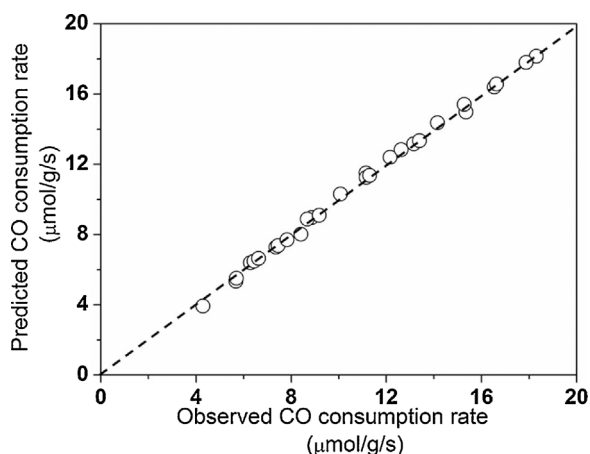


Fig. 15. Parity plot of measured and predicted CO consumption rates on Co₃O₄-In₂O₃ nanorod catalysts at 358 K using the kinetic parameters given in Table S3.

conversions were kept below 15% when reporting the reaction rate.

Based on the results of the effects of CO and O₂ pressure (Fig. 14), the CO oxidation rates could be described as Scheme 1. The first two steps in Scheme 1 represent the quasi-equilibrated binding of CO and O₂ molecules on vacant sites (*) to form CO* and O₂*, respectively (step 1 and 2). The next step takes place via the quasi-equilibrated reaction of surface adsorbed CO* and O₂* to form CO₃* (step 3). The formed CO₃* could finally react with adsorbed CO* in an irreversible step to generate CO₂ (step 4). The assumption of pseudo-steady state for all the adsorbed species and quasi-equilibrium for step 1, 2 and 3 leads to Eq. (4) of CO oxidation reaction. The kinetic parameters of K₁, K₂, K₃, and k₄ could be solved based on the measured reaction rate in Fig. 14 regressed using Eq. (4), and the results are summarized in Table S3. Eq. (4) could accurately describe (R² = 0.998) the measured reaction rate in Fig. 14. The accuracy of the rate equation could also be confirmed by the parity plots of the observed and calculated reaction rate as shown in Fig. 15. These mechanistic speculations are consistent with the FTIR results. Only stable carbonate species were observed over Co₃O₄-In₂O₃ nanorods that might be further reduced by CO to form the final product of CO₂.

$$r_{\text{CO}} = \frac{K_1^2 K_2 K_3 k_4 [\text{CO}]^2 [\text{O}_2]}{\{1 + K_1 [\text{CO}] + K_2 [\text{O}_2] + K_1 K_2 K_3 [\text{CO}] [\text{O}_2]\}^2} \quad (4)$$

$\begin{matrix} * & \text{CO}^* & \text{O}_2^* & \text{CO}_3^* \end{matrix}$

Based on the results of the effects of C₃H₆ pressure (Fig. 16(a)), it was observed that the reaction order was zero for C₃H₆ pressure, which immediately ruled out the possibility that C₃H₆ was involved in the rate-determining step. It was speculated that neither C₃H₆ adsorption nor the surface reaction of adsorbed C₃H₆ species and O₂ could govern the reaction rate of C₃H₆ oxidation [52]. The active sites on catalyst surface should be totally covered by the intermediates of C₃H₆ or its generated species, which actually acted as the most abundant surface intermediates (MASI). FTIR results confirmed that C₃H₆ and its related intermediates like formate, acetate, and acetone species would be formed over Co₃O₄-In₂O₃ nanorods. Since the reaction order was approximately 0.5 for O₂ pressure (Fig. 16(b)), the incorporation of activated oxygen into an anion vacancy sites was the kinetically-relevant step for C₃H₆ oxidation as shown in Scheme 2.

V represents the anion vacancies on the catalyst surface. The reaction rate of C₃H₆ oxidation (r_{C₃H₆}) is assumed to follow the equation of

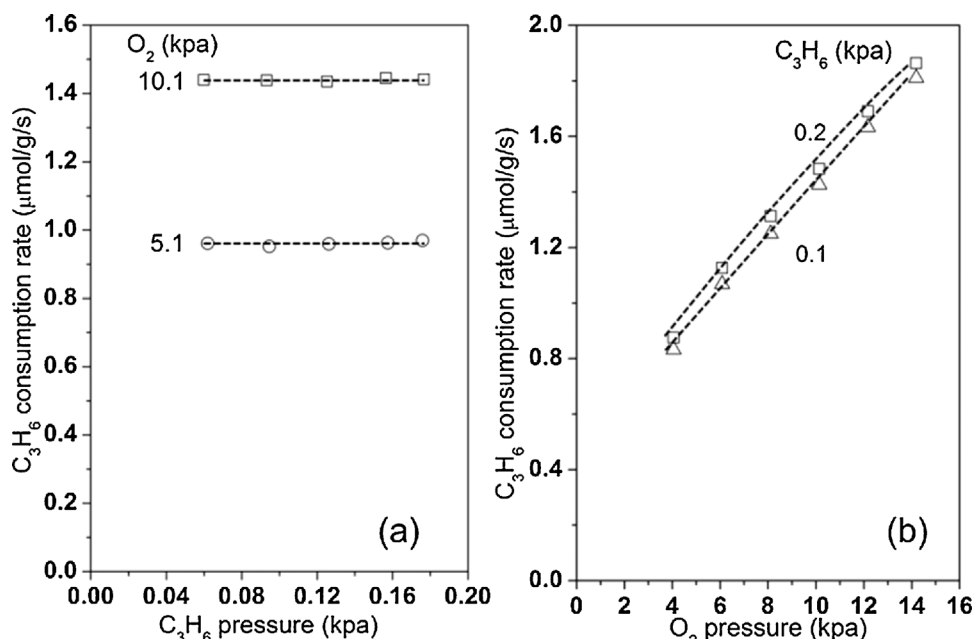
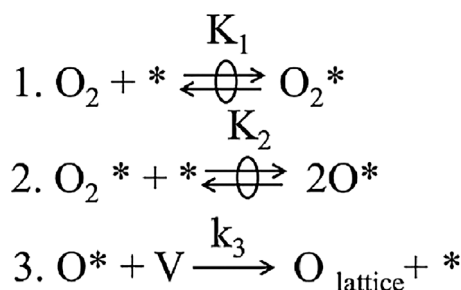


Fig. 16. Effects of C₃H₆ (a) and O₂ (b) pressures on C₃H₆ consumption rate on Co₃O₄-In₂O₃ nanorod catalysts at 476 K.



Scheme 2. The elementary step of oxygen activation during C₃H₆ catalytic oxidation.

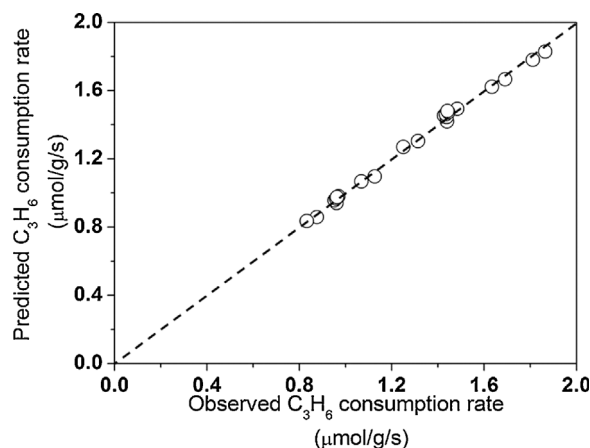


Fig. 17. Parity plot of measured and predicted C₃H₆ consumption rates on Co₃O₄-In₂O₃ nanorod catalysts at 476 K using the kinetic parameters given in Table S4.

$r_{\text{C}_3\text{H}_6} = k [\text{C}_3\text{H}_6]^\alpha [\text{O}_2]^\beta$, where α value should be zero. Then, the kinetic parameters of α , β and k could be solved based on the measured reaction rate in Fig. 16 by multiple linear regressions according to Eq. (5), and the results are summarized in Table S4. The $r_{\text{C}_3\text{H}_6}$ solved by Eq. (5) could accurately describe ($R^2 = 0.996$) the measured reaction rate in Fig. 16. The accuracy of the rate equation could also be confirmed by the parity plots of the observed and calculated reaction rate as shown in Fig. 17.

$$\ln(r_{\text{C}_3\text{H}_6}) = \ln k + \alpha \times \ln[\text{C}_3\text{H}_6] + \beta \times \ln[\text{O}_2] \quad (5)$$

4. Conclusions

The remarkable catalytic performance and hydrothermal stability of indium-doped Co₃O₄ nanorods make it possible to use these nanorod catalysts in diesel emission control. These findings might open up a avenue for a new generation of DOCs comprised of non-noble metals for effective removal of CO and propylene. Different characterization results illustrate that indium with larger cation radius distorts the lattice structure of Co₃O₄ nanorods, and facilitates the formation of oxygen vacancies involved in the catalytic oxidation reaction. The detailed reaction mechanism and kinetic rate laws for the oxidation reactions of CO and C₃H₆ are proposed, which are entirely consistent with the experimental observations. For CO oxidation, the activated CO₃* reduced by adsorbed CO* could be considered as the kinetically-relevant step. Only stable carbonate species are observed over Co₃O₄-In₂O₃ nanorods that would be further reduced by CO to form CO₂. For C₃H₆ oxidation, the incorporation of activated oxygen (O*) into anion vacancy of catalyst surface is the kinetically-relevant step, while C₃H₆ and its related intermediates like formate, acetate, and acetone species would be formed over Co₃O₄-In₂O₃ nanorods.

Acknowledgements

L.M. acknowledges financial support from State Key Joint Laboratory of Environment Simulation and Pollution Control (13K04ESPCT) and international postdoctoral exchange fellowship program (20140054). We thank Dr. Shuai Wang at Xiamen University for his comments and advice on the study, and also thank Dr. Haiping Sun at the University of Michigan for assistance in transmission electron microscopy experiments. The Kratos Axis Ultra XPS, the JEOL 2010F, and JEOL 3100R05 instruments were funded by NSF grants #DMR-0420785, #DMR-9871177, and #DMR-0723032, respectively.

Appendix A. Supplementary data

Supplementary data associated with this article can be found, in the online version, at <http://dx.doi.org/10.1016/j.apcatb.2017.10.001>.

References

- [1] A. Russell, W.S. Epling, Diesel oxidation catalysts, *Catal. Rev.* 53 (2011) 337–423.
- [2] H.-W. Jen, J.W. Girard, G. Cavataio, M.J. Jagner, Detection, origin and effect of ultra-low platinum contamination on diesel-SCR catalysts, *SAE Int.* 1 (2008) 1553–1559.
- [3] S.E. Voltz, C.R. Morgan, D. Liederman, S.M. Jacob, Kinetic study of carbon monoxide and propylene oxidation on platinum catalysts, *Ind. Eng. Chem. Prod. Res. Dev.* 12 (1973) 294–301.
- [4] J. Jones, H. Xiong, A.T. DeLaRiva, E.J. Peterson, H. Pham, S.R. Challa, G. Qi, S. Oh, M.H. Wiebenga, X.I. Pereira Hernández, Y. Wang, A.K. Datye, Thermally stable single-atom platinum-on-ceria catalysts via atom trapping, *Science* 353 (2016) 150–154.
- [5] C.H. Kim, G. Qi, K. Dahlberg, W. Li, Strontium-doped perovskites rival platinum catalysts for treating NO_x in simulated diesel exhaust, *Science* 327 (2010) 1624–1627.
- [6] W. Wang, G. McCool, N. Kapur, G. Yuan, B. Shan, M. Nguyen, U.M. Graham, B.H. Davis, G. Jacobs, K. Cho, X. Hao, Mixed-phase oxide catalyst based on Mn-mullite (Sm, Gd)Mn₂O₅ for NO oxidation in diesel exhaust, *Science* 337 (2012) 832–835.
- [7] Y.-F.Y. Yao, The oxidation of hydrocarbons and CO over metal oxides: III. Co₃O₄, *J. Catal.* 33 (1974) 108–122.
- [8] H.-F. Wang, R. Kavanagh, Y.-L. Guo, Y. Guo, G. Lu, P. Hu, Origin of extraordinarily high catalytic activity of Co₃O₄ and its morphological chemistry for CO oxidation at low temperature, *J. Catal.* 296 (2012) 110–119.
- [9] L.F. Liotta, H. Wu, G. Pantaleo, A.M. Venezia, Co₃O₄ nanocrystals and Co₃O₄-MO_x binary oxides for CO, CH₄ and VOC oxidation at low temperatures: a review, *Catal. Sci. Technol.* 3 (2013) 3085–3102.
- [10] A.J. Binder, T.J. Toops, R.R. Unocic, J.E. Parks, S. Dai, Low-temperature CO oxidation over a ternary oxide catalyst with high resistance to hydrocarbon inhibition, *Angew. Chem. Int. Ed.* 54 (2015) 13263–13267.
- [11] X. Xie, Y. Li, Z.-Q. Liu, M. Haruta, W. Shen, Low-temperature oxidation of CO catalysed by Co₃O₄ nanorods, *Nature* 458 (2009) 746–749.
- [12] Y. Lou, J. Ma, X. Cao, L. Wang, Q. Dai, Z. Zhao, Y. Cai, W. Zhan, Y. Guo, P. Hu, G. Lu, Y. Guo, Promoting effects of In₂O₃ on Co₃O₄ for CO oxidation: tuning O₂ activation and CO adsorption strength simultaneously, *ACS Catal.* 4 (2014) 4143–4152.
- [13] M. Zhou, L. Cai, M. Bajdich, M. García-Melchor, H. Li, J. He, J. Wilcox, W. Wu, A. Vojvodic, X. Zheng, Enhancing catalytic CO oxidation over Co₃O₄ nanowires by substituting Co²⁺ with Cu²⁺, *ACS Catal.* 5 (2015) 4485–4491.
- [14] M. Choi, W. Heo, F. Kleitz, R. Ryoo, Facile synthesis of high quality mesoporous SBA-15 with enhanced control of the porous network connectivity and wall thickness, *Chem. Commun.* (2003) 1340–1341.
- [15] A. Ruplecker, F. Kleitz, E.L. Salabas, F. Schuth, Hard templating pathways for the synthesis of nanostructured porous Co₃O₄, *Chem. Mater.* 19 (2007) 485–496.
- [16] A.-H. Lu, D. Zhao, Y. Wan, Appendix, Nanocasting: A Versatile Strategy for Creating Nanostructured Porous Materials, The Royal Society of Chemistry, 2009, pp. 246–253.
- [17] L. Glover, R. Douglas, G. McCullough, M. Keenan, P. Reverault, C. McAtee, Performance characterisation of a range of diesel oxidation catalysts: effect of Pt:Pd ratio on light off behaviour and nitrogen species formation, *SAE Int.* (2011).
- [18] M. Kruk, M. Jaroniec, C.H. Ko, R. Ryoo, Characterization of the porous structure of SBA-15, *Chem. Mater.* 12 (2000) 1961–1968.
- [19] K.S.W. Sing, D.H. Everett, R.A.W. Haul, L. Moscou, R.A. Pierotti, J. Rouquerol, T. Siemienińska, Reporting physisorption data for gas/solid systems with special reference to the determination of surface area and porosity (Recommendations 1984), *Pure Appl. Chem.* 57 (1985) 603–619.
- [20] E. Pellicer, M. Cabo, E. Rossinyol, P. Solsona, S. Suriñach, M.D. Baró, J. Sort, Nanocasting of mesoporous In-TM (TM = Co, Fe, Mn) oxides: towards 3D diluted-oxide magnetic semiconductor architectures, *Adv. Funct. Mater.* 23 (2013) 900–911.
- [21] S.-C. Chang, M.H. Huang, Formation of short In₂O₃ nanorod arrays within mesoporous silica, *J. Phys. Chem. C* 112 (2008) 2304–2307.
- [22] E.L. Salabas, A. Ruplecker, F. Kleitz, F. Radu, F. Schüth, Exchange anisotropy in nanocasted Co₃O₄ nanowires, *Nano Lett.* 6 (2006) 2977–2981.
- [23] J.P. Thielemann, F. Girgsdies, R. Schlögl, C. Hess, Pore structure and surface area of silica SBA-15: influence of washing and scale-up, *Beilstein J. Nanotechnol.* 2 (2011) 110–118.
- [24] Z. Chen, C.X. Kronawitter, B.E. Koel, Facet-dependent activity and stability of Co₃O₄ nanocrystals towards the oxygen evolution reaction, *Phys. Chem. Chem. Phys.* 17 (2015) 29387–29393.
- [25] D. Cabrera-German, G. Gomez-Sosa, A. Herrera-Gomez, Accurate peak fitting and subsequent quantitative composition analysis of the spectrum of Co 2p obtained with Al K α radiation: I: cobalt spinel, *Surf. Interface Anal.* 48 (2016) 252–256.
- [26] S.C. Pettito, E.M. Marsh, G.A. Carson, M.A. Langell, Cobalt oxide surface chemistry: the interaction of CoO(1 0 0), Co₃O₄(1 1 0) and Co₃O₄(1 1 1) with oxygen and water, *J. Mol. Catal. A: Chem.* 281 (2008) 49–58.
- [27] J. Yang, H. Liu, W.N. Martens, R.L. Frost, Synthesis and characterization of cobalt hydroxide, cobalt oxyhydroxide, and cobalt oxide nanodiscs, *J. Phys. Chem. C* 114 (2010) 111–119.
- [28] M.A. Langell, J.G. Kim, D.L. Pugmire, W. McCarroll, Nature of oxygen at rocksalt and spinel oxide surfaces, *J. Vac. Sci. Technol. A* 19 (2001) 1977–1982.
- [29] V. Christou, M. Etchells, O. Renault, P.J. Dobson, O.V. Salata, G. Beamson, R.G. Egdel, High resolution x-ray photoemission study of plasma oxidation of indium–tin–oxide thin film surfaces, *J. Appl. Phys.* 88 (2000) 5180–5187.
- [30] A. Bourlange, D.J. Payne, R.G. Palgrave, H. Zhang, J.S. Foord, R.G. Egdel, R.M.J. Jacobs, T.D. Veal, P.D.C. King, C.F. McConville, The influence of Sn doping on the growth of In₂O₃ on Y-stabilized ZrO₂(100) by oxygen plasma assisted molecular beam epitaxy, *J. Appl. Phys.* 106 (2009) 013703.
- [31] R.W. Hewitt, N. Winograd, Oxidation of polycrystalline indium studied by x-ray photoelectron spectroscopy and static secondary ion mass spectroscopy, *J. Appl. Phys.* 51 (1980) 2620–2624.
- [32] X. Xie, W. Shen, Morphology control of cobalt oxidenanocrystals for promoting their catalytic performance, *Nanoscale* 1 (2009) 50–60.
- [33] T.E. Davies, T. Garcia, B. Solsona, S.H. Taylor, Nanocrystalline cobalt oxide: a catalyst for selective alkane oxidation under ambient conditions, *Chem. Commun.* (2006) 3417–3419.
- [34] G. Fierro, M. Lo Jacono, M. Inversi, R. Dragone, P. Porta, TPR and XPS study of cobalt–copper mixed oxide catalysts: evidence of a strong Co–Cu interaction, *Top. Catal.* 10 (2000) 39–48.
- [35] G. Jacobs, Y. Ji, B.H. Davis, D. Cronauer, A.J. Kropf, C.L. Marshall, Fischer–Tropsch synthesis: temperature programmed EXAFS/XANES investigation of the influence of support type, cobalt loading, and noble metal promoter addition to the reduction behavior of cobalt oxide particles, *Appl. Catal. A: Gen.* 333 (2007) 177–191.
- [36] Z.P. Xu, H.C. Zeng, Interconversion of brucite-like and hydrotalcite-like phases in cobalt hydroxide compounds, *Chem. Mater.* 11 (1999) 67–74.
- [37] J. Feng, H.C. Zeng, Size-controlled growth of Co₃O₄ nanocubes, *Chem. Mater.* 15 (2003) 2829–2835.
- [38] M. Aghabaramnejad, G.S. Patience, J. Chaouki, TGA and kinetic modelling of Co, Mn and Cu oxides for chemical looping gasification (CLG), *Can. J. Chem. Eng.* 92 (2014) 1903–1910.
- [39] M.-Y. Kim, E.A. Kyriakidou, J.-S. Choi, T.J. Toops, A.J. Binder, C. Thomas, J.E. Parks II, V. Schwartz, J. Chen, D.K. Hensley, Enhancing low-temperature activity and durability of Pd-based diesel oxidation catalysts using ZrO₂ supports, *Appl. Catal. B: Environ.* 187 (2016) 181–194.
- [40] P. Thormählen, E. Fridell, N. Cruise, M. Skoglundh, A. Palmqvist, The influence of CO₂, C₃H₆ NO, H₂, H₂O or SO₂ on the low-temperature oxidation of CO on a cobalt–aluminate spinel catalyst (Co_{1.66}Al_{1.34}O₄), *Appl. Catal. B: Environ.* 31 (2001) 1–12.
- [41] K.I. Hadjiivanov, Identification of neutral and charged N_xO_y surface species by IR spectroscopy, *Catal. Rev.-Sci. Eng.* 42 (2000) 71–144.
- [42] W. Hertl, Infrared spectroscopic study of catalytic oxidation reactions over cobalt oxide under steady-state conditions, *J. Catal.* 31 (1973) 231–242.
- [43] H.-K. Lin, C.-B. Wang, H.-C. Chiu, S.-H. Chien, In situ FTIR study of cobalt oxides for the oxidation of carbon monoxide, *Catal. Lett.* 86 (2003) 63–68.
- [44] J. Fujita, A.E. Martell, K. Nakamoto, Infrared spectra of metal chelate compounds. VIII. Infrared spectra of Co(III) carbonate complexes, *J. Chem. Phys.* 36 (1962) 339–345.
- [45] A.J. Goodsel, Surface structures formed on cobalt oxide during catalytic oxidation: an infrared study, *J. Catal.* 30 (1973) 175–186.
- [46] G. Busca, V. Lorenzelli, Infrared spectroscopic identification of species arising from reactive adsorption of carbon oxides on metal oxide surfaces, *Mater. Chem.* 7 (1982) 89–126.
- [47] P. Pietrzyk, C. Dujardin, K. Gora-Marek, P. Granger, Z. Sojka, I.R. Spectroscopic, EPR, and operando DRIFT insights into surface reaction pathways of selective reduction of NO by propene over the Co-BEA zeolite, *Phys. Chem. Chem. Phys.* 14 (2012) 2203–2215.
- [48] J.L. Flores-Moreno, G. Delahay, F. Figueras, B. Coq, DRIFTS study of the nature and reactivity of the surface compounds formed by co-adsorption of NO, O₂ and propene on sulfated titania-supported rhodium catalysts, *J. Catal.* 236 (2005) 292–303.
- [49] P. Concepción, P. Botella, J.M.L. Nieto, Catalytic and FT-IR study on the reaction pathway for oxidation of propane and propylene on V- or Mo–V-based catalysts, *Appl. Catal. A: Gen.* 278 (2004) 45–56.
- [50] E. Finocchio, G. Busca, V. Lorenzelli, V.S. Escribano, FTIR studies on the selective oxidation and combustion of light hydrocarbons at metal oxide surfaces. Part 2. Propane and propene oxidation on Co₃O₄, *J. Chem. Soc. Faraday Trans.* 92 (1996) 1587–1593.
- [51] E. Finocchio, R.J. Willey, G. Busca, V. Lorenzelli, FTIR studies on the selective oxidation and combustion of light hydrocarbons at metal oxide surfaces Part 3. Comparison of the oxidation of C3 organic compounds over Co₃O₄, MgCr₂O₄ and CuO, *J. Chem. Soc. Faraday Trans.* 93 (1997) 175–180.
- [52] I.M. Campbell, *Catalysis at Surfaces*, Springer, Netherlands, 1988.